The Astrophysical Journal, 972:56 (20pp), 2024 September 1 https://doi.org/10.3847/1538-4357/ad5ae0

Lyα Emission Line Profiles of Extreme [O III]- emitting Galaxies at $z \gtrsim 2$: Implications for Lyα Visibility in the Reionization Era

Mengtao Tang[1,2], Daniel P. Stark[1], Richard S. Ellis[2], Michael W. Topping[1], Charlotte Mason[3], Zhihui Li[4], and Adèle Plat[5]
[1] Steward Observatory, University of Arizona, 933 N Cherry Avenue, Tucson, AZ 85721, USA
[2] Department of Physics and Astronomy, University College London, Gower Street, London WC1E 6BT, UK
[3] Cosmic Dawn Center (DAWN), Niels Bohr Institute, University of Copenhagen, Jagtvej 128, 2200 København N, Denmark
[4] Cahill Center for Astronomy and Astrophysics, California Institute of Technology, 1200 E California Boulevard, MC 249-17, Pasadena, CA 91125, USA
[5] Institute for Physics, Laboratory for Galaxy Evolution and Spectral Modelling, Ecole Polytechnique Federale de Lausanne, Observatoire de Sauverny, Chemin Pegasi 51, CH-1290 Versoix, Switzerland
Received 2024 April 9; revised 2024 June 13; accepted 2024 June 20; published 2024 August 23

Abstract

JWST observations have recently begun delivering the first samples of Lyα velocity profile measurements at $z > 6$, opening a new window into the reionization process. Interpretation of $z \gtrsim 6$ line profiles is currently stunted by limitations in our knowledge of the intrinsic Lyα profile (before encountering the intergalactic medium (IGM)) of the galaxies that are common at $z \gtrsim 6$. To overcome this shortcoming, we have obtained resolved ($R \sim 3900$) Lyα spectroscopy of 42 galaxies at $z = 2.1$–3.4 with similar properties as are seen at $z > 6$. We quantify a variety of Lyα profile statistics as a function of [O III]+Hβ equivalent width (EW). Our spectra reveal a new population of $z \simeq 2$–3 galaxies with large [O III]+Hβ EWs (>1200 Å) and a large fraction of Lyα flux emerging near the systemic redshift (peak velocity $\simeq 0$ km s^{-1}). These spectra indicate that low-density neutral hydrogen channels are able to form in a subset of low-mass galaxies ($\lesssim 1 \times 10^8\,M_\odot$) that experience a burst of star formation (sSFR > 100 Gyr^{-1}). Other extreme [O III] emitters show weaker Lyα that is shifted to higher velocities ($\simeq$240 km s^{-1}) with little emission near the line center. We investigate the impact the IGM is likely to have on these intrinsic line profiles in the reionization era, finding that the centrally peaked Lyα emitters should be strongly attenuated at $z \gtrsim 5$. We show that these line profiles are particularly sensitive to the impact of resonant scattering from infalling IGM and can be strongly attenuated even when the IGM is highly ionized at $z \simeq 5$. We compare these expectations against a new database of $z \gtrsim 6.5$ galaxies with robust velocity profiles measured with JWST/NIRSpec.

Unified Astronomy Thesaurus concepts: Galaxies (573); High-redshift galaxies (734); Reionization (1383); Observational cosmology (1146)

1. Introduction

Studying the reionization of hydrogen in the intergalactic medium (IGM) provides important clues to understanding the early history of cosmic structure formation. Over the past two decades, numerous observational efforts have been devoted to studying the connection between galaxy formation and cosmic reionization (Stark 2016; Robertson 2022). Lyα emission lines from high-redshift galaxies provide a useful tool to probe the neutral hydrogen (H I) in the IGM (Dijkstra 2014; Ouchi et al. 2020). Because of the strong cross section for scattering with neutral hydrogen, Lyα photons emitted from galaxies at redshifts where the IGM is mostly neutral should be strongly suppressed (e.g., Miralda-Escudé 1998; McQuinn et al. 2007; Mesinger et al. 2015).

Spectroscopic observations have revealed that the fraction of galaxies showing prominent Lyα emission (e.g., with equivalent width EW > 25 Å) declines significantly from $z \simeq 6$ to $z \gtrsim 7$, consistent with expectations if the IGM is highly neutral (neutral fraction $x_{\rm HI} \gtrsim 0.5$) at $z \gtrsim 7$ and becomes highly ionized at $z \simeq 6$ (e.g., Stark et al. 2010; Caruana et al. 2014; Schenker et al. 2014; Pentericci et al. 2018; Mason et al. 2019; Jones et al. 2024; Nakane et al. 2024). Such evolution is also supported by studies of the abundance of narrowband-selected Lyα emitters at $z > 5.5$ (e.g., Ouchi et al. 2010; Ota et al. 2017; Zheng et al. 2017; Itoh et al. 2018; Konno et al. 2018; Goto et al. 2021). This time line of reionization is consistent with constraints from measurements of the electron scattering optical depth of the cosmic microwave background (Planck Collaboration et al. 2020) and quasar absorption spectra, which suggest that the IGM is substantially neutral at $z \gtrsim 7$ (e.g., Bañados et al. 2018; Davies et al. 2018; Yang et al. 2020a; Wang et al. 2020; Greig et al. 2022) and is significantly ionized at $z \simeq 5$–6 (e.g., McGreer et al. 2015; Yang et al. 2020b; Bosman et al. 2021; Jin et al. 2023; Zhu et al. 2023; see Fan et al. 2023 for a review).

Over the last decade, attention has begun to focus on using Lyα measurements to trace the local reionization process around galaxies at $z \gtrsim 7$. Observations have revealed that many ultraviolet (UV) luminous ($M_{\rm UV} \lesssim -21.5$) galaxies at $z \gtrsim 7$ have visible Lyα emission (e.g., Oesch et al. 2015; Zitrin et al. 2015; Roberts-Borsani et al. 2016; Stark et al. 2017; Larson et al. 2022; Cooper et al. 2024). It has been suggested that these systems trace overdense regions with a high density of faint neighboring galaxies (e.g., Tilvi et al. 2020; Jung et al. 2022; Leonova et al. 2022; Whitler et al. 2023a; Chen et al. 2024), which are able to power large ionized bubbles (e.g., Wyithe & Loeb 2005; Dayal et al. 2009; Castellano et al. 2016; Weinberger et al. 2018; Endsley & Stark 2022). In this case, Lyα photons will be significantly redshifted before

encountering the neutral IGM, boosting the transmission of the line (e.g., Mesinger et al. 2004; Mason & Gronke 2020; Qin et al. 2022; Smith et al. 2022; Napolitano et al. 2024). There is also evidence that the Lyα peak of these galaxies is offset to a high velocity from the systemic redshift, shifting the Lyα photons far into the damping wing before encountering the neutral IGM (e.g., Stark et al. 2017; Tang et al. 2023). This further boosts the transmission of Lyα, countering the attenuation provided by the neutral IGM (e.g., Mason et al. 2018b; Endsley et al. 2022). Efforts are underway to link Lyα emission in these systems to bubble sizes (e.g., Hayes & Scarlata 2023; Lu et al. 2024), but such estimates rely on knowledge of how much Lyα is redshifted relative to the galaxy systemic redshift.

Spectroscopy with JWST (Gardner et al. 2023) NIRSpec (Jakobsen et al. 2022) has recently pushed the Lyα frontier beyond $z \simeq 10$ (Bunker et al. 2023a), while also delivering the first large samples of Lyα profile measurements at $z \gtrsim 7$ (e.g., Bunker et al. 2023a; Tang et al. 2023; Saxena et al. 2024). Some $z \gtrsim 7$ galaxies have been detected with Lyα EWs $\simeq$ 10–20 Å and relatively large Lyα peak velocity offsets ($\gtrsim$400 km s^{-1}; e.g., Bunker et al. 2023a; Tang et al. 2023), similar to the luminous galaxies studied prior to JWST (e.g., Stark et al. 2017; Endsley et al. 2022). However, JWST has also revealed the discovery of a new class of systems at $z \gtrsim 7$ (Saxena et al. 2023; Chen et al. 2024), with extremely strong Lyα emission (EW $\simeq$ 300–400 Å), which may be escaping with low Lyα velocity offsets ($\simeq$100 km s^{-1}). If such strong Lyα is observed near the systemic redshift, it would require that the emitting galaxy resides in a large ionized region ($R \gtrsim 3$ pMpc; Saxena et al. 2023), allowing the line profile to escape with minimal processing by the IGM.

Reliably linking Lyα velocity offsets to constraints on bubble sizes relies on knowledge of the full range of factors modulating the Lyα profiles in reionization-era galaxies. Before Lyα photons encounter the IGM, the H I distribution in the ISM and the circumgalactic medium (CGM) resonantly scatters the Lyα photons emitted from H II regions. The profiles we are now observing at $z \gtrsim 7$ will have been further altered by scattering from the neutral IGM. Even at $z \simeq 5$ when the IGM is highly ionized, the residual H I in the IGM will attenuate the Lyα emission near the line center via resonant scattering (e.g., Gunn & Peterson 1965). Without a detailed understanding of the range of intrinsic[6] Lyα spectral shapes in galaxies typical of the reionization era, it is difficult to reliably assess the impact of the IGM on the observed Lyα profiles at $z \gtrsim 6$, stunting efforts to infer ionized bubble sizes around known Lyα emitters.

High-resolution ($R \gtrsim 4000$) Lyα spectroscopy of galaxies at lower redshifts ($z \simeq 2$–3) provides our best path toward understanding the range of intrinsic Lyα profiles that are likely present in reionization-era galaxies. While such spectra have been obtained for typical galaxies at $z \simeq 2$–3 (e.g., Shapley et al. 2003; Steidel et al. 2010; Erb et al. 2014; Trainor et al. 2015; Matthee et al. 2021), they do not exist for galaxies with properties similar to that seen at $z \gtrsim 6$. In this paper, we seek to build such a Lyα spectral library at $z \simeq 2$–3. A key feature of reionization-era galaxies is intense [O III]+Hβ line emission (with median rest-frame EW $z \simeq$ 700–800 Å; e.g., Labbé et al. 2013; De Barros et al. 2019; Endsley et al. 2021b, 2023a), as expected in moderately metal-poor systems with young stellar populations. Du et al. (2020) and Tang et al. (2021a) have presented a first step toward studying the Lyα emission of this population, with medium-resolution ($R \simeq 1000$) Lyα spectroscopy of $z \sim 2$–3 extreme emission line galaxies (EELGs) spanning the full range of [O III]+Hβ EWs expected at $z \simeq 7$–8 (EW$_{\rm [O\,III]+H\beta}$$\simeq$300–3000 Å; e.g., Endsley et al. 2021b, 2023a). In this work, we present high-resolution ($R \simeq 4000$) spectroscopy of 42 EELGs at $z = 2.1$–3.4, enabling the characterization of resolved line profiles. Using this data set, we explore the range of Lyα profiles seen in galaxies with different [O III]+Hβ EWs. The data set allows insight into the intrinsic Lyα profiles (and hence the H I distribution) that are likely in reionization-era galaxies. We use our spectral library to discuss how the $z \gtrsim 5$ IGM is likely to alter these line profiles. We compare these expectations against the existing sample of $z \gtrsim 6.5$ Lyα emitters with robust velocity profiles from JWST/NIRSpec grating spectroscopy.

The organization of this paper is as follows. In Section 2, we describe the observations and the resolved Lyα spectroscopy of $z = 2.1$–3.4 EELGs. We present the Lyα profiles of sources in our sample and discuss the constraints on the H I distribution in Section 3. We then discuss the implications for the Lyα profiles of $z \gtrsim 7$ galaxies and the Lyα visibility in the reionization era in Section 4. Finally, we summarize our conclusions in Section 5. We adopt a Λ-dominated, flat universe with $\Omega_\Lambda = 0.7$, $\Omega_{\rm M} = 0.3$, and $H_0 = 70$ km s^{-1} Mpc^{-1}. All magnitudes in this paper are quoted in the AB system Oke & Gunn (1983), and all EWs are quoted in the rest frame.

2. Observations and Analysis

In this work, we aim to characterize the Lyα emission line profiles of low-mass galaxies with extreme [O III] emission lines at $z \simeq 2$–3 using high-resolution ($R \simeq 4000$) spectroscopy. We describe the sample selection and spectroscopic observations in Section 2.1, and then present the resolved Lyα profiles in Section 2.2.

2.1. Spectroscopic Observations

The Lyα spectra studied in this paper follow a large rest-frame optical spectroscopic survey of EELGs at $z = 1.3$–3.7 (Tang et al. 2019, 2022) in the Cosmic Assembly Near-infrared Deep Extragalactic Legacy Survey (Grogin et al. 2011; Koekemoer et al. 2011) fields. The sample of EELGs was identified based on the [O III] EWs inferred from Hubble Space Telescope (HST) grism spectra (at $z = 1.3$–2.4) or the K-band flux excess (at $z = 3.1$–3.7). EELGs are required to have large rest-frame [O III] $\lambda\lambda$4959, 5007 EWs with values $\simeq$300–3000 Å, which are chosen to match the range expected to be common in reionization-era galaxies (e.g., Endsley et al. 2023a). Sources that harbor active galactic nuclei were removed based on their X-ray detections by matching the coordinates to the Chandra X-ray catalogs. We direct the reader to Tang et al. (2019) for the full description of the EELG sample selection. A low-resolution ($R \simeq 1000$) rest-frame UV spectroscopic study of the EELGs has been presented in Tang et al. (2021a, 2021b). Here, we measure the Lyα line profiles of EELGs using high-resolution spectroscopy.

The resolved Lyα spectra of EELGs were taken from the Binospec (Fabricant et al. 2019) on the MMT telescope with multislit spectroscopy mode. We utilized the 1000 line mm^{-1} grism blazed at 13°.75 with wavelength coverage from 3700 to

[6] In this paper, we define the intrinsic Lyα profile as that which emerges from the ISM and CGM of the host galaxy prior to interaction with the IGM.

5400 Å (centered at 4500 Å). This wavelength range allows us to measure Lyα emission line at $z = 2.1$–3.4. We designed one multislit mask in the Ultra Deep Survey (UDS) field (centered at R.A. = 02:17:26.8 and decl. = −05:18:52.0 with position angle PA = −78°), targeting 44 EELGs at $z = 2.1$–3.4 to measure their Lyα emission. The HST $i_{\rm F814W}$ magnitudes of these 44 targets range from 23.9 to 26.9 AB mag with a median of $i_{\rm F814W} = 25.5$, corresponding to absolute UV magnitudes $M_{\rm UV} = -21.7$ to -18.1 (median $M_{\rm UV} = -19.5$). We also filled the mask with 16 EELGs at lower redshift ($z = 1.4$–2) to measure C III] emission, thereby continuing our ongoing survey targeting UV metal emission lines in EELGs (Tang et al. 2021b). The targets were placed on the mask using the selection function introduced in Tang et al. (2019, 2021b). The target priority was adjusted based on their [O III] EWs, and those with the largest EWs ([O III]+Hβ EW > 1500 Å) were given the highest priority as they are very rare and have rest-frame optical spectral properties similar to the luminous Lyα emitters at $z > 7$ (e.g., Roberts-Borsani et al. 2016; Stark et al. 2017; Tang et al. 2023). We observed this mask between September and November 2021 with a total on-target integration time of 16 hr during an average seeing of 1.″0. The slit width was set to 1.″0, resulting in a spectral resolution of $R = 3900$ (corresponding to $\sigma_{\rm instrument} = 33$ km s^{-1}), which allows us to resolve the multipeak nature of Lyα emission line.

We reduced the Binospec spectra using the publicly available data reduction pipeline[7] (Kansky et al. 2019). The pipeline performs flat-fielding, wavelength calibration, sky subtraction, and then the 2D spectra extraction. The 1D spectra extraction and flux calibration were performed following the procedures described in Tang et al. (2021b). We created 1D spectra from the reduced 2D spectra using a boxcar extraction. We observed spectrophotometric standard stars and the instrumental response was corrected using the sensitivity curve-derived observations of standard stars. Slit-loss correction was performed using the in-slit light fraction computed from the HST image following the procedures described in Kriek et al. (2015). We then performed the absolute flux calibration using observations of slit stars, by comparing the slit-loss corrected count rates of slit star spectra with the broadband flux in the Skelton et al. (2014) catalogs.

Our goal is to measure the Lyα line profiles in EELGs at $z = 2.1$–3.4, which can be used as analogs of reionization-era systems. The 44 targets in our sample span a wide range of [O III]+Hβ EW (=342–2541 Å), typical of values expected at $z > 6$ (e.g., Endsley et al. 2023a). We derive the stellar population properties (stellar mass, stellar age, and specific star formation rate (sSFR)) of the 44 targets by fitting the broadband photometry from the Skelton et al. (2014) catalogs and available emission line fluxes using the BEAGLE tool (Chevallard & Charlot 2016) assuming constant star formation history (CSFH; see Tang et al. 2019, 2021b for details of modeling procedures). BEAGLE uses the latest version of Bruzual & Charlot (2003) stellar population models and combines it with Cloudy (Ferland et al. 2013) to compute the nebular emission following the methods in Gutkin et al. (2016). The intense rest-frame optical emission of our targets indicates young ages (≃2–200 Myr) and large sSFRs (≃4–400 Gyr^{-1}). The stellar mass of our sample spans from $10^{7.5}\,M_\odot$ to $10^{9.5}\,M_\odot$. Galaxies with larger [O III] EWs tend to be lower mass (assuming CSFH) systems with larger sSFRs (left and middle panels of Figure 1). The median [O III]+Hβ EW and sSFR of our sample are 883 Å and 54 Gyr^{-1}, which are much larger than the average values of typical $z \sim 2$–3 galaxies (e.g., Reddy et al. 2012; Mármol-Queraltó et al. 2016; Santini et al. 2017; Boyett et al. 2022) but more comparable to typical galaxies at $z \sim 7$–8 (Labbé et al. 2013; De Barros et al. 2019; Endsley et al. 2021b, 2023a). In particular, our sample includes 13 galaxies with very intense optical line emission (EW$_{\rm [O\ III]+H\beta}$>1200 Å), a population that is extremely rare at $z \sim 2$–3 (Boyett et al. 2022) but becomes more common in the reionization era (Smit et al. 2015; Endsley et al. 2021b, 2023a; Bouwens et al. 2023). The light of such galaxies is dominated by very young stellar populations ($\lesssim$10 Myr assuming CSFH, though older stellar populations could be outshined by young stars; e.g., Tang et al. 2022; Whitler et al. 2023b), as expected for systems that have recently experienced extreme bursts of star formation.

We also derive the hydrogen ionizing photon production efficiency ($\xi_{\rm ion}$) of our targets from BEAGLE models. Here, we use $\xi_{\rm ion}$ defined as the hydrogen ionizing photon production rate ($\dot{N}_{\rm ion}$) per dust-corrected luminosity at rest frame 1500 Å ($L_{\rm UV}$, including nebular and stellar continuum; see Chevallard et al. 2018; Tang et al. 2019 for various definitions of $\xi_{\rm ion}$). The $\xi_{\rm ion}$ of the 44 targets ranges from $10^{25.3}$ to $10^{25.9}$ erg^{-1} Hz. For the subset with Hβ and Hα emission line measurement, we compare their $\xi_{\rm ion}$ derived from dust-corrected Hα luminosity plus $L_{\rm UV}$ (Tang et al. 2019) and from BEAGLE models. We find both values are consistent. The $\xi_{\rm ion}$ of our sample is higher than the $\xi_{\rm ion}$ of typical star-forming galaxies at $z \sim 2$ (e.g., Matthee et al. 2017; Shivaei et al. 2018) but comparable to $z > 6$ sources (e.g., Stark et al. 2017; Endsley et al. 2021b; Stefanon et al. 2022; Ning et al. 2023; Simmonds et al. 2023; Tang et al. 2023), indicating that our EELGs have intense ionizing spectra similar to that seen in the reionization era.

We identify Lyα emission lines and compute the Lyα fluxes and EWs by applying the procedures described in Tang et al. (2021a). Using the redshifts derived by fitting [O III] λ5007 emission lines from the ground-based (26 galaxies; Tang et al. 2019) or HST grism-based (18 galaxies; Momcheva et al. 2016) rest-frame optical spectra, we visually inspect the expected positions of Lyα in the 2D Binospec spectra. Out of the total 44 EELGs at $z = 2.1$–3.4 on the mask, we have detected Lyα emission with S/N > 3 in 42 sources. For the remaining two sources lacking Lyα detections, we estimate 3σ upper limits for the Lyα flux and EW.

The Lyα fluxes are measured from the 1D spectra (examples shown in Figures 2 and 3). Due to the complex profile of resolved Lyα emission, we compute the line fluxes for the 42 galaxies with Lyα detections by directly integrating the flux between rest frame 1212 and 1220 Å. This wavelength window captures the total Lyα flux for all Lyα-emitting sources (e.g., Du et al. 2020; Matthee et al. 2021). The measured Lyα fluxes are from 2.4×10^{-18} to 4.2×10^{-16} erg s^{-1} cm^{-2}. For the remaining two galaxies without Lyα detection, the 3σupper limit of Lyα flux is derived by integrating the error spectrum in quadrature over rest frame 1199.9–1228.8 Å (Kornei et al. 2010). The 3σ Lyα flux limits of these two objects are 2.0×10^{-17} and 2.9×10^{-17} erg s^{-1} cm^{-2}.

Using the measured Lyα fluxes, we compute the Lyα escape fraction for a subset with Hβ and Hα measurement in our

[7] https://bitbucket.org/chil_sai/binospec

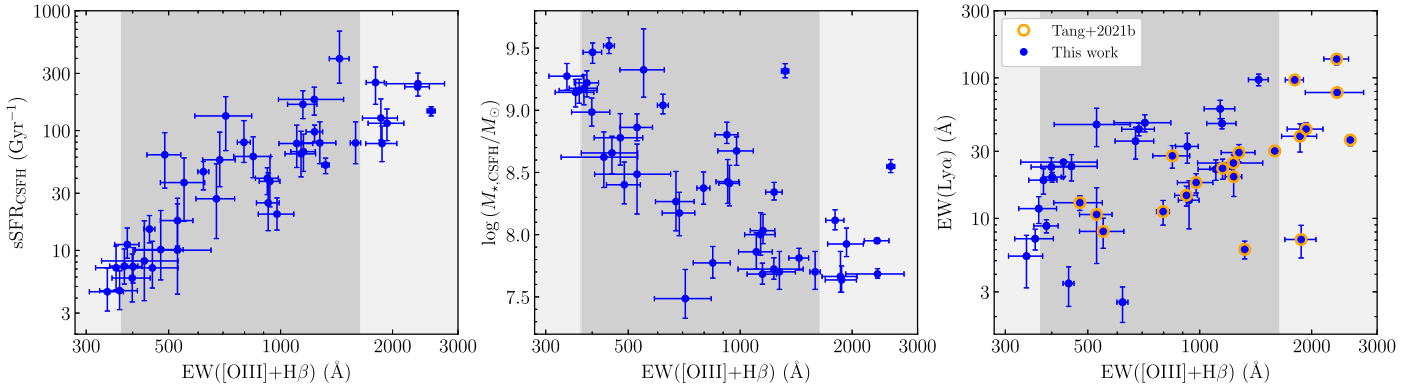

Figure 1. sSFR (left panel), stellar mass (middle panel), and Lyα EW (right panel) as a function of [O III]+Hβ EW for galaxies in our resolved Lyα spectroscopic sample at $z = 2.1$–3.4. Stellar masses and sSFRs are derived from the BEAGLE models assuming CSFH. In the right panel, objects that have already obtained low-resolution Lyα spectra in Tang et al. (2021a) are marked by orange open circles. We mark the [O III]+Hβ EW range that is typical at $z > 6$ with the dark gray (68% within the median value) and the light gray shaded regions (95% within the median) based on the [O III]+Hβ EW distribution at $z > 6$ presented in Endsley et al. (2023a). Galaxies with larger [O III]+Hβ EWs tend to have larger sSFRs, lower stellar masses, and stronger Lyα emission.

sample (eight galaxies; Tang et al. 2019). The Lyα escape fraction ($f_{\rm esc,Ly\alpha}$) is calculated from the ratio of observed Lyα luminosity to the intrinsic Lyα luminosity ($L_{\rm Ly\alpha,int}$). We derive the intrinsic Lyα flux from the dust-corrected Hα luminosity assuming case B recombination ($L_{\rm Ly\alpha,int} = 8.7 \times L_{\rm H\alpha,corrected}$, e.g., Hayes et al. 2010; Erb et al. 2014; Henry et al. 2015; Trainor et al. 2015; Jaskot et al. 2019). The derived $f_{\rm esc,Ly\alpha}$ ranges from 0.05 to 0.41.

The Lyα emission line EWs are computed from the measured Lyα line fluxes and the underlying continuum flux densities. Due to the lack of high S/N (>5) continuum measurement in our Binospec spectra, we estimate the continuum flux density using the broadband photometry in Skelton et al. (2014) catalogs. We fit the broadband fluxes from filters covering the rest frame 1250–2600 Å with a power law $f_\lambda \propto \lambda^\beta$ (Calzetti et al. 1994). Then, using the fitted $f_\lambda - \lambda$ relation we derive the average flux density at rest frame 1225–1250 Å as the continuum flux density (Kornei et al. 2010; Stark et al. 2010). Dividing the measured Lyα flux by the continuum flux density, the Lyα EWs of the 42 galaxies with Lyα detections in our sample are from 1 to 136 Å with a median of 23 Å.

The relationship between Lyα EW and [O III]+Hβ EW is shown in the right panel of Figure 1. We find that the Lyα EW increases with the [O III]+Hβ EW as has been shown previously (Du et al. 2020; Tang et al. 2021a). The median Lyα EW ranges from 12 Å at EW$_{\rm [O\,III]+H\beta}$ = 300–500 Å to 18 Å at EW$_{\rm [OIII]+H\beta}$ = 500–1000 Å to 25 Å at EW$_{\rm [OIII]+H\beta}$ = 1000–1500 Å. For galaxies with the largest [O III]+Hβ EWs in our sample (=1500–3000 Å), the median Lyα EW is much larger (=41 Å). Galaxies with such extremely large [O III] +Hβ EW become much more common at $z > 6$ (e.g., Smit et al. 2015; Endsley et al. 2021b, 2023a; Boyett et al. 2024). While there are also moderately strong Lyα emitters (EW$_{\rm Ly\alpha}$ = 3–40 Å) at EW$_{\rm [O\,III]+H\beta}$>1500 Å, we start seeing extremely strong Lyα (EW$_{\rm Ly\alpha}$ = 70–150 Å) among these very intense optical line emitters. Overall, we have obtained high-resolution Lyα spectra for sources spanning [O III]+Hβ EW = 300–3000 Å, allowing investigation of the Lyα profiles in galaxies with similar properties as those found in the reionization era.

2.2. Lyα Profile Measurements

In this section, we characterize the Lyα line profiles of our sample of EELGs. Of the 42 sources with Lyα in emission, 30 show a faint blue peak and a brighter red peak. One object presents a more complex Lyα profile (UDS-07665) with three peaks (Figure 2), similar to that seen in the Sunburst Arc (Rivera-Thorsen et al. 2017). The remaining 11 EELGs in our sample show single-peaked Lyα lines.

We first consider the velocity offset of the Lyα peak redshift and the systemic redshift ($v_{\rm peak}$). The Lyα velocity offset is sensitive to the column density of H I on the far side of the galaxy (e.g., Verhamme et al. 2006, 2015), providing an indirect probe of the transmission of Lyα photons, assuming a symmetric distribution of H I (e.g., Verhamme et al. 2008). Computing $v_{\rm peak}$ requires precise measurement of the systemic redshift ($z_{\rm sys}$). At $z = 2.1$–3.4, the red end of Binospec grating used in this work cuts off at $\lesssim$rest frame 1650 Å. With this wavelength coverage, it is not possible to recover systemic redshifts (via nonresonant UV emission lines; i.e., O III], C III]) using the Binospec spectra. Instead, we use the bright (and high S/N) [O III] or Hα emission lines detected in near-infrared (NIR) spectra with relatively high resolution ($R > 1000$) to derive systemic redshifts. Out of the 42 EELGs at $z = 2.1$–3.4, [O III] or Hα emission have been detected in 26 galaxies from our ground-based spectroscopic campaign (Tang et al. 2019).

To ensure our systemic redshift measurements are robust, we examine the consistency of systemic redshifts derived between Binospec and NIR spectra. Although we are not able to derive systemic redshifts for our $z = 2.1$–3.4 objects from our Binospec spectra, we take advantage of lower redshift ($z = 1.4$–1.7) sources with spectra obtained from the same Binospec and NIR multislit observations. For these $z = 1.4$–1.7 galaxies, we derive systemic redshifts based on resolved C III] detections in Binospec spectra, and [O III] or Hα detections in NIR spectra (Tang et al. 2019) separately. We find that the systemic redshift derived from Binospec and NIR spectra are consistent, with a systematic uncertainty of $\simeq$40 km s^{-1}, similar to the Binospec spectra resolution. This suggests the systemic redshifts derived from NIR spectra in Tang et al. (2019) should be sufficiently robust in inferring the Lyα peak velocity offsets for our $z = 2.1$–3.4 EELGs.

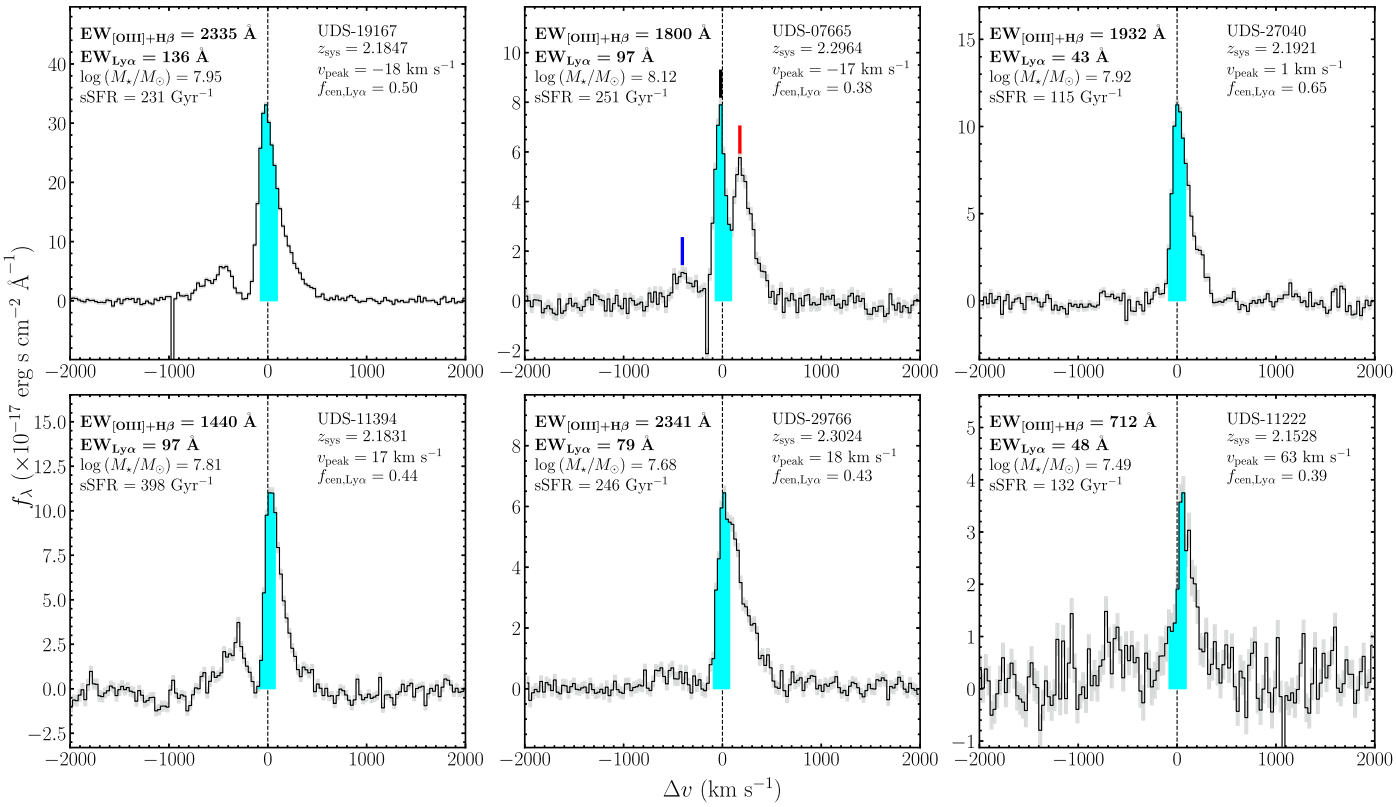

Figure 2. Lyα emission profiles of the six EELGs with high Lyα central escape fractions ($f_{\rm cen,Ly\alpha} \gtrsim 0.4$) and strong Ly$\alpha$ emission (EW$_{\rm Ly\alpha} > 40$ Å) at our $z = 2.1$–3.4 sample. Cyan shaded regions marking the Lyα photons emitting within ± 100 km s^{-1} of the systemic redshift (black dashed line). Their Lyα peaks are close to the systemic redshifts ($v_{\rm peak} < 100$ km s^{-1}), potentially indicating ionized channels in the ISM and the CGM that allow Lyα to escape directly into the IGM. UDS-07665 has a triple-peak Lyα profile, with the blue, central, and red peaks marked by the blue, black, and red lines.

We derive the Lyα peak offset by measuring the shift of the Lyα profile maximum with respect to the systemic redshift. For the 26 EELGs at $z = 2.1$–3.4 with systemic redshift measurements, their Lyα peak offsets range from $v_{\rm peak} = -18$ to 594 km s^{-1}. In the left panel of Figure 4, we plot Lyα peak offset as a function of [O III]+Hβ EW.

We also measure the velocity separation between the blue and red Lyα peaks ($S_{\rm peak}$), which has been widely studied in literature and has been shown to correlate with $N_{\rm HI}$ and the ionizing photon escape fraction (e.g., Verhamme et al. 2015; Izotov et al. 2018, 2021; Flury et al. 2022; Hu et al. 2023; Pahl et al. 2024). For the 30 double-peaked Lyα emitters in our sample, the Lyα peak separations range from 316 to 846 km s^{-1}. For the triple-peaked Lyα emitter UDS-07665, we measure the separation between the two peaks blueward and redward the central peak, resulting in $S_{\rm peak} = 582$ km s^{-1}. However, 11 out of the 42 sources in our sample only show a single-peaked Lyα profile, preventing us from accurately measuring their peak separations. These objects may have faint and hence undetected blue peaks, or very small peak separations which are not resolved in the spectra. To avoid introducing any bias into our results, we will primarily focus on the Lyα peak offset $v_{\rm peak}$ in this work, although we will also briefly discuss our peak separation $S_{\rm peak}$ measurements.

We next consider the fraction of Lyα emission within ± 100 km s^{-1} of the systemic velocity (the Lyα "central escape fraction," $f_{\rm cen,Ly\alpha}$, as defined in Naidu et al. 2022) in order to constrain the H I covering fraction. In a clumpy H I distribution, Lyα photons can escape directly through low-opacity ($\tau \ll 1$, or equivalently $N_{\rm HI} \lesssim 10^{13}$ cm^{-2}; e.g., Dijkstra 2016; Ouchi et al. 2020) channels, as may be expected if a subset of the massive stars is (partially) covered by low-density H I with highly ionized sightlines (e.g., Gazagnes et al. 2020; Ma et al. 2020). This results in a significant fraction of the Lyα line emerging at the systemic redshift, as shown in both simulations (e.g., Behrens et al. 2014; Verhamme et al. 2015; Dijkstra et al. 2016) and observations (e.g., Rivera-Thorsen et al. 2017). When computing $f_{\rm cen,Ly\alpha}$ (=Lyα flux at ± 100 km s^{-1}/total Lyα flux), we choose the same central velocity window (± 100 km s^{-1}) as in Naidu et al. (2022) since both samples have a similar spectral resolution ($R \simeq 4000$) around Lyα (Matthee et al. 2021). We show $f_{\rm cen,Ly\alpha}$ as a function of [O III] +Hβ EW in the right panel of Figure 4. For the 26 EELGs with $z_{\rm sys}$ in our sample, the measured Lyα central escape fraction ranges from $f_{\rm cen,Ly\alpha} < 0.02$ (3σ upper limit) to $f_{\rm cen,Ly\alpha} = 0.65$.

The flux ratio of blue to red Lyα peaks (so-called "blue-to-red ratio") also provides constrains the H I and dust content. Since the blueshifted Lyα emission faces significant scattering through the near side of the galaxy, a larger blue-to-red flux ratio may imply a low $N_{\rm H\,I}$ and less dust. We measure the blue-to-red Lyα ratio for the 30 EELGs with double-peaked Lyα emission in our sample. The median blue-to-red ratio of these 30 objects is 0.29, which is consistent with the average blue-to-red flux ratio of Lyα emission lines of Lyα-emitting galaxies at $z \sim 2$–3 (e.g., Trainor et al. 2015; Hayes et al. 2021; Matthee et al. 2021).

Finally, we quantify the full width at half-maximum (FWHM) of the Lyα profile for our EELGs to provide a measurement of the width of red Lyα damping wings. The FWHM is computed by subtracting the instrument resolution in

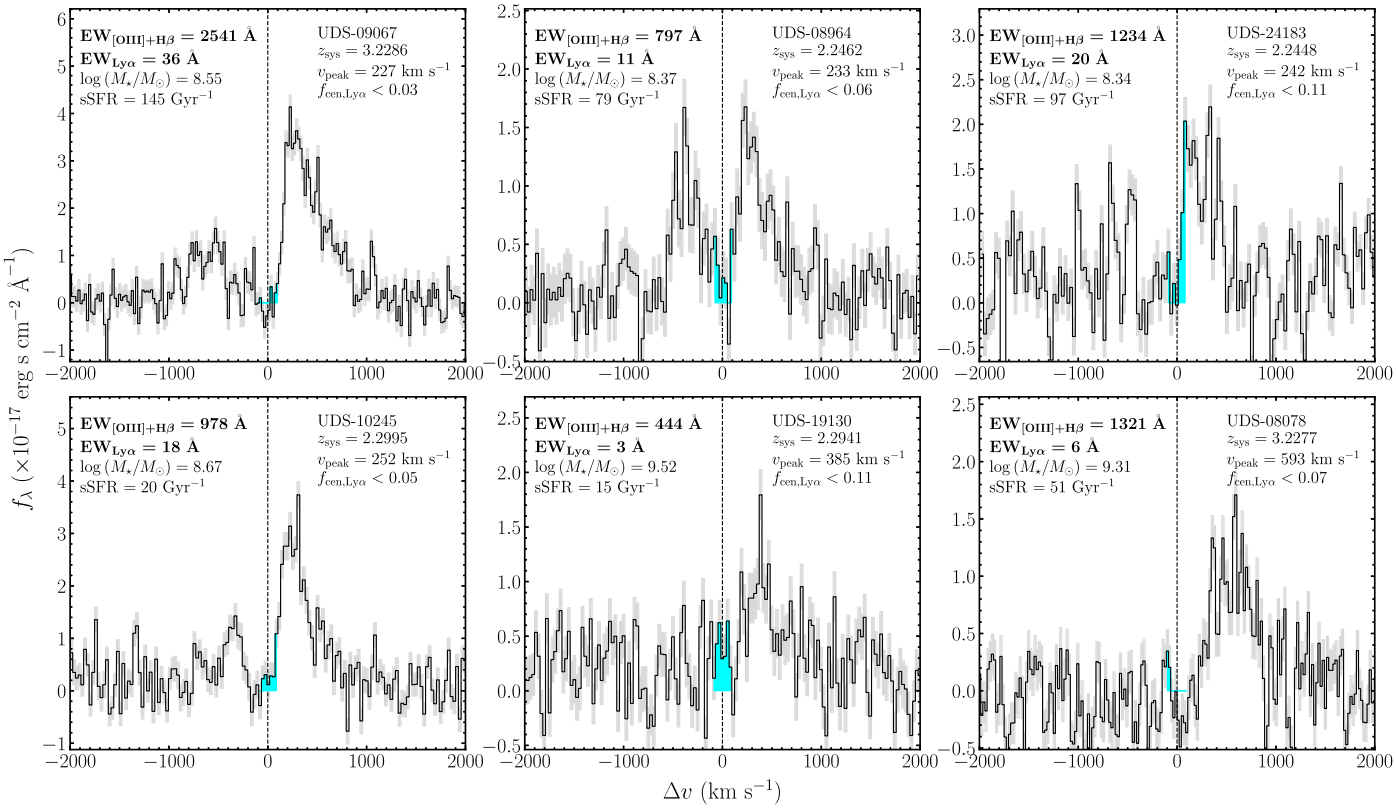

Figure 3. Examples of Lyα emission profiles of our $z = 2.1$–3.4 EELGs with moderate Lyα emission ($EW_{Ly\alpha} = 3$–40 Å), which emit negligible Lyα flux near (within ± 100 km s^{-1}) the line center (cyan shaded regions). Spectra are plotted in a similar way as in Figure 2. Their Lyα peaks are shifted to relatively large velocities ($\gtrsim$200 km s^{-1}), indicating that the H II regions are likely covered by denser H I gas.

quadrature from the observed FWHM. For the 30 double-peaked Lyα emitters in our sample, the median FWHMs of blue-peak and red-peak Lyα emission are 264 km s^{-1} and 290 km s^{-1}, respectively. For the 11 single-peaked Lyα emitters, the median FWHM is 316 km s^{-1}. Since the blue-shifted Lyα emission is more likely to be affected by the residual neutral hydrogen in the IGM, we quote the FWHM as the FWHM of the red-peak emission for double-peaked Lyα emitters, or the FWHM of the entire emission for single-peaked Lyα emitters in the following. We summarize the Lyα profile measurements of our $z = 2.1$–3.4 EELGs in Table 1.

3. Lyα in Extreme [O III] Emitters

The spectra described in the previous section allow us to characterize the Lyα profiles in $z \simeq 2$–3 galaxies with extremely large [O III]+Hβ EWs, a population of low-mass galaxies with large sSFR, similar to what is commonly seen in the reionization era. While Lyα profiles are potentially useful for insight into Lyman continuum (LyC) escape in this population (e.g., Verhamme et al. 2015, 2017; Izotov et al. 2018; Rivera-Thorsen et al. 2019; Gazagnes et al. 2020; Flury et al. 2022; Naidu et al. 2022; Pahl et al. 2024), our primary focus in this paper is on developing a baseline for interpreting the database of $z \gtrsim 7$ line profiles now emerging from JWST observations. We begin in Section 3.1 by describing the properties of galaxies with significant Lyα transmission at the line center, potentially signaling very low-density (and highly ionized) channels facilitating the direct escape of Lyα. We then describe the range of Lyα profiles seen in galaxies as a function of [O III]+Hβ EW, first considering values that are typical of the reionization era (400–1200 Å; Section 3.2). We close by discussing the Lyα profiles of $z \simeq 2$–3 galaxies with [O III] +Hβ EW > 1200 Å (Section 3.3).

3.1. Lyα Profiles with Large Central Escape Fractions

Recently, attention has focused on the subset of galaxies with Lyα photons directly escaping near (± 100 km s^{-1}) the line center (e.g., Rivera-Thorsen et al. 2017; Naidu et al. 2022). One possible explanation for such line profiles is partial coverage of neutral hydrogen, with holes that allow transmission of Lyα at the systemic redshift. Naidu et al. (2022) have characterized the central flux fraction of Lyα ($f_{cen,Ly\alpha}$; see Section 2.2 for definition) for a sample of $z = 0$–4 galaxies with LyC leakage, with the results showing large $f_{cen,Ly\alpha}$ values (0.1–0.4) in the strongest leakers (e.g., Naidu et al. 2017; Rivera-Thorsen et al. 2019; Izotov et al. 2021; Matthee et al. 2021). Analysis of $z \simeq 2$ galaxies selected on strong Lyα also reveals a subset with emission near the line center, with values reaching as high as $f_{cen,Ly\alpha} = 0.2$–0.5 (Naidu et al. 2022). Interest in this subclass of the Lyα emitter population is partially driven by their potential as LyC leaking candidates given the very low H I column density implied by direct Lyα escape[8] (Naidu et al. 2022; Choustikov et al. 2024). Recent work has also highlighted the utility of this population for probing the IGM at $z \gtrsim 7$ (Saxena et al. 2023; Tang et al. 2024).

[8] Large values of $f_{cen,Ly\alpha}$ may alternatively be driven by very small separation of the blue and red peaks (i.e., $S_{peak} \lesssim 100$ km s^{-1}), with the majority of flux emerging close to the line center. This case also requires low H I column densities (albeit not as low as required for direct escape) and may be linked to significant LyC escape. We will comment on this later in the section.

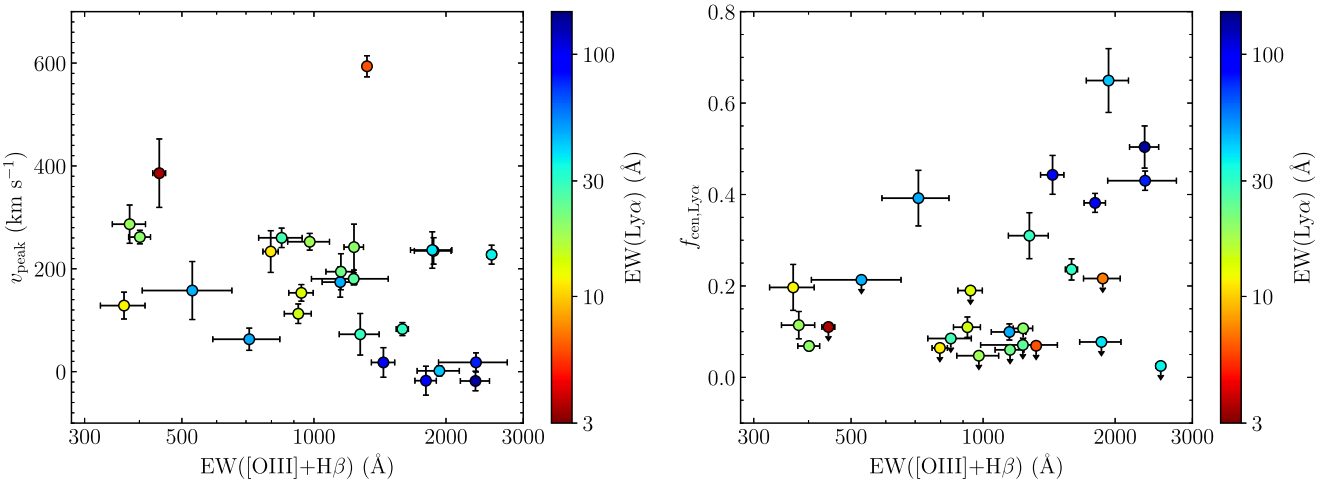

Figure 4. Lyα peak velocity offset (v_{peak}; left panel) and Lyα central escape fraction ($f_{cen,Ly\alpha}$; right panel) as a function of [O III]+Hβ EW for the 26 EELGs at $z = 2.1$–3.4 with systemic redshift measurement in our sample. Data are color-coded by Lyα EWs. Galaxies with small v_{peak} (<100 km s^{-1}) and large $f_{cen,Ly\alpha}$ (>0.2) are found to have the largest [O III]+Hβ EWs (>1200 Å) and large Lyα EWs (>40 Å).

Since significant transmission near the systemic redshift is only expected in large ionized regions (e.g., Mason & Gronke 2020), the identification of $z \gtrsim 7$ galaxies with both large $f_{cen,Ly\alpha}$ (or small v_{peak}) and large Lyα escape fractions enables constraints on the proximity of the galaxy to neutral hydrogen in the IGM (e.g., Prieto-Lyon et al. 2023; Lu et al. 2024).

The low-density (and highly ionized) sightlines that facilitate Lyα with large $f_{cen,Ly\alpha}$ (e.g., Behrens et al. 2014; Erb et al. 2014; Verhamme et al. 2015; Dijkstra et al. 2016) have been suggested to arise shortly after the intense bursts of star formation (e.g., Smith et al. 2019; Ma et al. 2020) that appear fairly ubiquitously at $z \gtrsim 6$ (e.g., Labbé et al. 2013; Smit et al. 2014; Endsley et al. 2021b; Topping et al. 2022; Endsley et al. 2023a; Whitler et al. 2023a). Our sample (selected on [O III] +Hβ EW) allows us to quantify how commonly Lyα has large central flux fractions in low-mass galaxies experiencing rapid upturns of star formation at $z \simeq 2$–3. Figure 2 shows the six galaxies with the largest Lyα central flux fractions in our high-resolution MMT spectra. The values spanned in these galaxies ($f_{cen,Ly\alpha} = 0.38$–0.65) are as large as any of the LyC leakers and Lyα emitters considered in Naidu et al. (2022), potentially indicating that EELGs (at least occasionally) produce very low H I density channels that allow direct escape of Lyα.

The spectral energy distributions (SEDs) of the six large $f_{cen,Ly\alpha}$ systems are shown in Figure 5. The UV continuum slopes of these galaxies are relatively blue (median $\beta = -2.3$), indicating low dust attenuation. The galaxies have among the largest [O III]+Hβ EWs in the sample (EW = 712–2341 Å, with a median EW $\simeq$1900 Å). The light-weighted ages of the six galaxies are correspondingly young, ranging from 2 to 8 Myr, with a median of 4 Myr (all assuming CSFH). The stellar masses are low, ranging from 3×10^7 to $1 \times 10^8\,M_\odot$. The derived sSFRs (115–400 Gyr^{-1}) point to galaxies caught in the midst of a significant burst of star formation. The existence of strong and centrally peaked Lyα emission in this subset of galaxies may indicate that low H I density channels can form quickly in low-mass galaxies during intense star formation episodes. This is consistent with the short timescale of forming low-density channels ($\simeq$1–3 Myr) indicated by hydrodynamical simulations (e.g., Ma et al. 2020; Kakiichi & Gronke 2021). We will show in Sections 3.2 and 3.3 that these conditions only occur in a subset of the extreme [O III]-emitting population, suggesting that not all low-mass galaxies have extremely low-density neutral gas along our sightline during large sSFR phases.

We expect the six galaxies in our sample with centrally prominent Lyα emission to have large Lyα EWs, both because of the effective transmission implied by the line profile and the efficient ionizing photon production implied by the young stellar population ages. This is indeed the case, with the majority showing intense Lyα emission (median EW = 90 Å). The Lyα escape fractions derived from Hα (see Section 2.1) indicate larger-than-average transmission relative to typical continuum-selected galaxies (e.g., Hayes et al. 2010; Erb et al. 2014; Matthee et al. 2016; Sobral et al. 2017), with a median value of $f_{esc,Ly\alpha} = 0.22$ (ranging from $f_{esc,Ly\alpha} = 0.16$ to 0.41). The Lyα escape fractions are slightly lower than those of Green Peas with similar Lyα EWs (median $f_{esc,Ly\alpha} = 0.3$; Yang et al. 2017), likely because the emission from diffuse Lyα halos is not fully recovered by the 1″ width Binospec slit (e.g., Lujan Niemeyer et al. 2022). Yet in spite of these enhanced values, the escape fractions imply that the majority of the Lyα emission is not detected, as would be expected if the low H I density gas (that permits transmission near the line center) is surrounded by denser gas which does scatter Lyα photons.

The Lyα profiles offer further insight into the mode of Lyα escape in galaxies with centrally peaked Lyα emission. In addition to the prominent central component, we generally also see a blue peak and red tail of emission extending to higher velocities (100–400 km s^{-1}). This confirms the suggestion that a significant fraction of the Lyα photons arrive via resonant scattering or backscattering through dense H I, also indicating that the lower H I density gas (that permit emission at systemic) is likely surrounded by denser gas (which scatters Lyα photons to larger velocities).

The Lyα spectrum of UDS-07665 ([O III]+Hβ = 1800 Å, $f_{cen,Ly\alpha} = 0.38$) provides an illustrative example. The Lyα profile shows three components with a central peak close to the systemic, similar to that seen in some known LyC leakers (and strong Lyα emitters) at $z = 0$–4, including the Sunburst Arc (Rivera-Thorsen et al. 2017), J1243 + 4646 (Izotov et al. 2018), and Ion3 (Vanzella et al. 2018). The central component

Table 1
Lyα Properties of the 42 Galaxies with Lyα Emission Detection in Our Sample

Target ID	R.A. (hh:mm:ss)	Decl. (dd:mm:ss)	z_{sys}	λ_{blue} (Å)	λ_{red} (Å)	$F_{Ly\alpha,blue}$ ($\times10^{-18}$ cgs)	$F_{Ly\alpha,red}$ ($\times10^{-18}$ cgs)	$EW_{Ly\alpha}$ (Å)	FWHM (km s^{-1})	v_{peak} (km s^{-1})	$f_{cen,Ly\alpha}$	$EW_{[O\,III]+H\beta}$ (Å)
UDS-19835	02:17:01.94	−05:12:35.47	...	3880.75	3888.33	13.28 ± 2.59	26.18 ± 3.36	8.8 ± 0.9	333 ± 32	...	...	387 ± 29
UDS-32530	02:17:04.81	−05:10:02.64	2.1512	3828.39	3832.46	2.10 ± 4.11	31.74 ± 6.08	11.7 ± 2.5	385 ± 56	128 ± 26	0.20 ± 0.05	369 ± 43
UDS-09067	02:17:01.48	−05:14:45.36	3.2286	5129.98	5144.48	18.86 ± 4.75	58.38 ± 5.03	36.1 ± 3.2	417 ± 27	227 ± 18	<0.03	2541 ± 63
UDS-08078	02:17:02.74	−05:14:57.50	3.2277	...	5149.66	...	22.34 ± 3.22	6.0 ± 0.9	414 ± 45	593 ± 20	<0.07	1321 ± 30
UDS-22025	02:17:06.36	−05:12:06.88	...	...	3849.48	...	16.27 ± 1.94	12.9 ± 1.5	542 ± 95	...	...	476 ± 71
UDS-27576	02:17:08.11	−05:10:59.82	...	3860.37	3867.61	14.57 ± 7.71	33.27 ± 6.63	23.4 ± 5.0	349 ± 52	...	...	452 ± 78
UDS-21302	02:17:07.94	−05:12:15.51	2.1804	3862.43	3868.35	8.46 ± 3.35	10.50 ± 4.69	46.6 ± 14.1	288 ± 95	157 ± 56	<0.21	528 ± 122
UDS-11049	02:17:07.14	−05:14:19.88	...	3932.50	3937.91	6.67 ± 1.19	44.58 ± 13.02	35.5 ± 9.0	263 ± 28	...	...	672 ± 80
UDS-33286	02:17:12.40	−05:09:52.91	...	3995.26	4003.77	1.85 ± 0.96	14.13 ± 4.42	2.5 ± 0.7	266 ± 34	...	...	620 ± 21
UDS-32404	02:17:13.54	−05:10:02.79	...	...	3816.50	...	14.04 ± 7.75	10.7 ± 5.9	280 ± 117	...	...	528 ± 53
UDS-37633	02:17:16.05	−05:08:57.44	...	3754.76	3759.57	19.10 ± 9.46	57.09 ± 15.72	32.5 ± 7.8	331 ± 32	...	...	926 ± 65
UDS-23016	02:17:15.48	−05:11:55.36	2.1541	3830.98	3838.01	11.75 ± 5.72	39.79 ± 8.90	18.7 ± 3.8	504 ± 84	286 ± 37	0.11 ± 0.03	380 ± 33
UDS-21724	02:17:20.01	−05:12:10.62	3.2279	5128.57	5141.15	5.68 ± 1.61	28.17 ± 2.29	30.2 ± 2.5	410 ± 25	82 ± 12	0.24 ± 0.02	1591 ± 51
UDS-14097	02:17:22.44	−05:13:42.89	2.1565	3833.94	3839.49	8.52 ± 2.55	43.36 ± 3.54	47.3 ± 4.0	258 ± 16	174 ± 29	0.10 ± 0.02	1148 ± 104
UDS-10245	02:17:22.93	−05:14:30.63	2.2995	4006.73	4014.48	8.42 ± 3.17	39.98 ± 6.89	18.0 ± 2.8	289 ± 27	252 ± 16	<0.05	978 ± 107
UDS-10805	02:17:23.71	−05:14:22.97	2.2924	3999.70	4004.88	12.20 ± 3.30	19.70 ± 3.03	24.8 ± 3.5	129 ± 14	180 ± 11	<0.07	1232 ± 245
UDS-15533	02:17:26.08	−05:13:25.28	2.1572	3832.82	3840.60	16.79 ± 5.50	36.39 ± 6.72	22.7 ± 3.7	342 ± 52	194 ± 35	<0.06	1152 ± 87
UDS-14425	02:17:26.38	−05:13:40.64	2.2103	3897.36	3906.07	21.71 ± 4.28	68.22 ± 5.70	19.7 ± 1.6	339 ± 20	261 ± 13	0.07 ± 0.01	401 ± 23
UDS-27411	02:17:29.13	−05:11:01.46	2.2096	...	3902.76	...	28.72 ± 4.03	29.4 ± 4.1	316 ± 33	72 ± 40	0.31 ± 0.05	1275 ± 133
UDS-18860	02:17:29.26	−05:12:45.54	2.2103	...	3905.72	...	9.54 ± 2.49	7.1 ± 1.8	191 ± 35	234 ± 25	<0.22	1874 ± 180
UDS-04725	02:17:27.93	−05:15:37.62	...	4022.27	4027.08	8.97 ± 4.18	27.28 ± 4.33	22.4 ± 3.7	228 ± 25	...	...	1105 ± 115
UDS-27009	02:17:33.88	−05:11:06.40	...	...	3900.54	...	72.30 ± 10.87	60.1 ± 9.0	319 ± 36	...	...	1135 ± 107
UDS-11394	02:17:32.18	−05:14:16.25	2.1831	3865.76	3869.83	31.09 ± 8.88	96.78 ± 8.23	97.0 ± 9.2	190 ± 15	17 ± 28	0.44 ± 0.04	1440 ± 88
UDS-13231	02:17:33.19	−05:13:53.71	...	...	4006.36	...	12.34 ± 5.00	5.4 ± 2.2	228 ± 72	...	...	342 ± 36
UDS-27151	02:17:36.14	−05:11:06.18	2.1538	3828.76	3835.42	15.09 ± 8.23	59.66 ± 8.77	14.6 ± 2.3	344 ± 37	112 ± 18	0.11 ± 0.02	921 ± 65
UDS-07665	02:17:33.78	−05:15:02.85	2.2964	4001.92	4007.10	12.06 ± 2.52	93.85 ± 4.74	96.6 ± 4.9	...	−17 ± 28	0.38 ± 0.02	1800 ± 101
UDS-13128	02:17:35.23	−05:13:54.79	...	3836.90	3841.34	15.96 ± 12.35	13.31 ± 7.53	50.9 ± 25.1	145 ± 57	...	...	430 ± 100
UDS-05713	02:17:36.23	−05:15:26.38	...	...	4048.17	...	9.02 ± 1.51	7.2 ± 1.2	...	...	...	361 ± 43
UDS-22650	02:17:39.96	−05:11:59.00	2.1708	3853.18	3857.99	3.74 ± 2.29	26.80 ± 5.09	27.8 ± 5.1	256 ± 31	260 ± 18	<0.09	844 ± 96
UDS-11222	02:17:39.10	−05:14:17.88	2.1528	3824.82	3833.57	8.84 ± 3.78	30.11 ± 3.89	47.9 ± 6.7	221 ± 21	63 ± 21	0.39 ± 0.06	712 ± 124
UDS-29766	02:17:43.46	−05:10:33.45	2.3024	4007.06	4014.87	6.39 ± 2.42	74.06 ± 2.70	78.6 ± 3.5	290 ± 7	18 ± 18	0.43 ± 0.02	2341 ± 418
UDS-23682	02:17:43.01	−05:11:47.56	...	...	3939.78	...	2.39 ± 0.99	0.9 ± 0.4	...	...	...	488 ± 51
UDS-27040	02:17:44.29	−05:11:06.22	2.1921	...	3880.56	...	103.60 ± 11.08	43.2 ± 4.6	201 ± 5	1 ± 9	0.65 ± 0.07	1932 ± 213
UDS-19167	02:17:43.54	−05:12:43.61	2.1847	3866.13	3871.31	67.63 ± 7.50	352.90 ± 37.72	136.1 ± 12.4	234 ± 5	−18 ± 18	0.50 ± 0.05	2335 ± 178
UDS-29927	02:17:46.26	−05:10:32.68	2.1987	3880.06	3890.55	2.93 ± 3.10	16.97 ± 6.77	13.5 ± 5.0	181 ± 27	153 ± 16	<0.19	936 ± 60
UDS-24183	02:17:47.40	−05:11:41.45	2.2448	3937.06	3947.79	8.36 ± 5.84	25.28 ± 7.29	19.8 ± 5.5	365 ± 81	242 ± 44	<0.11	1234 ± 63
UDS-20810	02:17:48.02	−05:12:20.91	2.2559	3953.08	3961.22	14.80 ± 4.37	10.55 ± 3.76	38.4 ± 8.7	252 ± 72	236 ± 35	<0.08	1861 ± 201
UDS-19130	02:17:51.10	−05:12:45.17	2.2941	...	4009.69	...	18.93 ± 5.95	3.4 ± 1.1	460 ± 123	385 ± 66	<0.11	444 ± 15
UDS-25351	02:17:54.23	−05:11:27.56	...	3854.66	3859.10	3.16 ± 2.43	29.62 ± 4.85	23.2 ± 3.8	311 ± 31	...	...	399 ± 47
UDS-06274	02:17:52.31	−05:15:20.26	...	4971.32	4983.90	1.62 ± 1.10	13.07 ± 3.38	8.1 ± 2.0	433 ± 78	...	...	550 ± 75
UDS-08728	02:17:56.20	−05:14:49.26	...	3942.35	3950.86	6.50 ± 3.72	47.72 ± 4.11	43.1 ± 4.4	254 ± 24	...	...	686 ± 69
UDS-08964	02:17:57.38	−05:14:45.59	2.2462	3941.24	3949.38	13.72 ± 4.57	20.04 ± 4.94	11.2 ± 2.2	335 ± 39	233 ± 40	<0.06	797 ± 32

Note. Systemic redshifts (z_{sys}) are computed by fitting [O III] λ5007 or Hα lines. For the 30 objects with double-peaked Lyα lines, the peak wavelengths and fluxes of blue and red peak Lyα are shown in λ_{blue}, λ_{red}, $F_{Ly\alpha,blue}$, and $F_{Ly\alpha,red}$. For the 11 objects with single-peaked Lyα emission, the central wavelengths and total fluxes are shown in λ_{red} and $F_{Ly\alpha,red}$. For UDS-07665, which shows triple-peaked Lyα, we show its central peak wavelength in λ_{red} and the total flux of the central and red peaks in $F_{Ly\alpha,red}$. Lyα EWs are given as the total Lyα EWs. FWHMs are computed for the entire Lyα emission for single-peaked Lyα-emitting galaxies, and for the red-peak Lyα emission for double-peaked Lyα-emitting galaxies. The flux units are erg s^{-1} cm^{-2} (cgs).

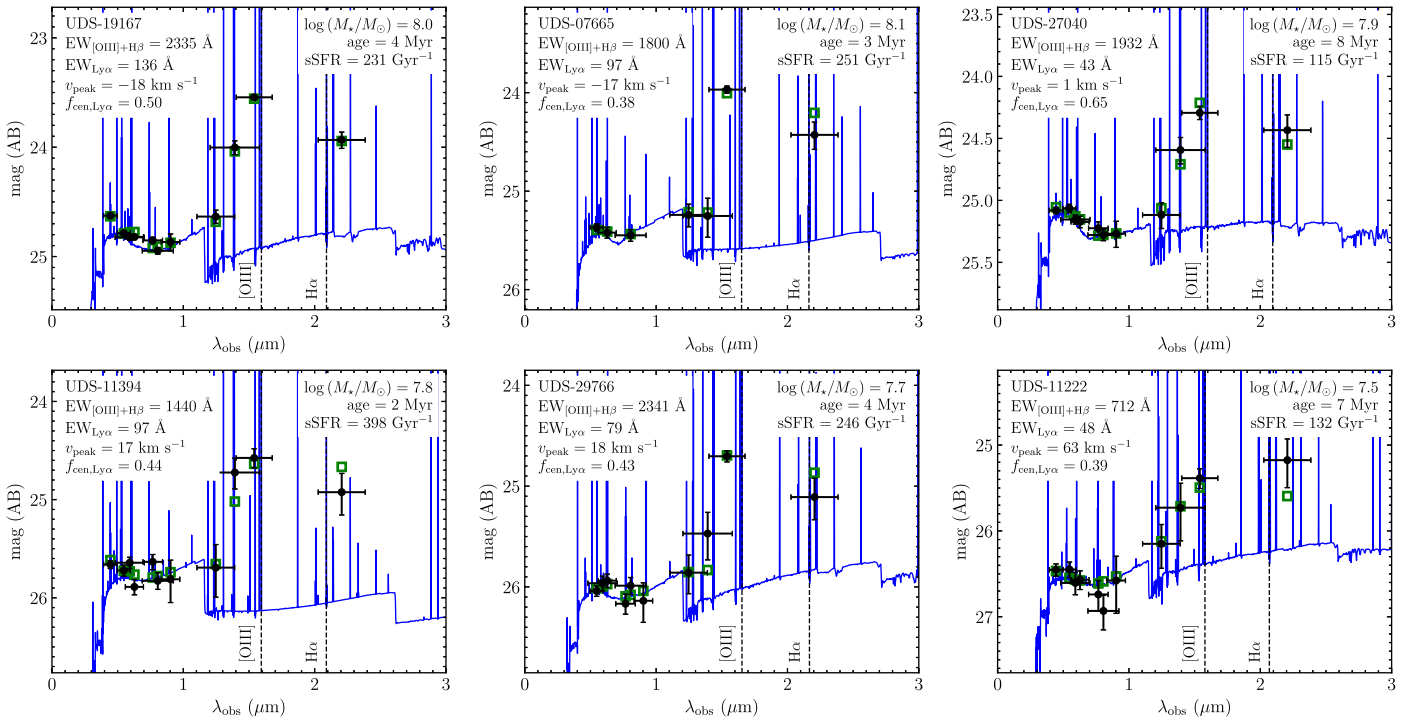

Figure 5. SEDs of the six galaxies with high Lyα central escape fraction ($f_{\rm cen,Ly\alpha} \gtrsim 0.4$) in our $z = 2.1$–3.4 EELG sample. Observed broadband photometry is shown as black-filled circles. The best-fit SED models inferred from BEAGLE are plotted by solid blue lines, and synthetic photometry is presented by open green squares. These objects are characterized by extremely young stellar populations (2–8 Myr assuming CSFH) and low stellar masses (3×10^7–$1 \times 10^8\ M_\odot$).

in UDS-07665 has a peak velocity of $v_{\rm peak} = -17$ km s^{-1} and narrow line width (FWHM = 74 km s^{-1}). The central Lyα component line width is comparable to that of the Hα emission line of UDS-07665 (FWHM = 88 km s^{-1} after subtracting the instrument resolution in quadrature) and also those of nonresonant rest-frame optical emission lines in similarly selected galaxies (e.g., Maseda et al. 2014; Tang et al. 2022), as would be expected if it arises via direct escape without scattering. The blue peak ($v = -405$ km s^{-1}) and red peak ($v = +177$ km s^{-1}) velocities are consistent with expectations for scattering through (and backscattering off of) dense outflowing neutral gas. Notably this implies that the separation between the red and blue peaks is large ($S_{\rm peak} = 582$ km s^{-1}), in spite of the presence of gas conditions that permit significant Lyα transmission at the line center. This underlies why peak separation is not a sufficient criterion for identifying galaxies with very low H I column density channels, as pointed out in Naidu et al. (2022) and Almada Monter & Gronke (2024).

In one case (UDS-27040), we do not see clearly defined and robustly detected blue peak. It is possible that the blue and red peaks are unresolved in this system, leading to the appearance of a single central peak. This may be expected if young stars are uniformly covered by slowly outflowing neutral hydrogen that has low column density yet is optically thick to Lyα (e.g., Verhamme et al. 2015). It is also possible that the S/N of this system is too low to recover the blue peak. In either case, this spectrum still implies at least partial coverage by low column densities of neutral hydrogen. For the six galaxies with large Lyα central escape fractions, we will use the radiative transfer models developed in Li et al. (2021), Li & Gronke (2022) to explore the physical conditions required to explain these line profiles in a future paper.

3.2. Lyα Profiles in Galaxies with [O III]+Hβ EW = 400–1200 Å

One of the primary goals of our observations is to obtain a census of Lyα profiles in $z \simeq 2$–3 galaxies with large [O III] +Hβ EWs. We begin by considering the 23 objects in our high-resolution sample with [O III]+Hβ EW = 400–1200 Å (with 11 of these having systemic redshift measurements). This range is fairly typical of galaxies in the reionization era, where the median (25th–75th percentile) [O III]+Hβ EW is 780 Å (500–1220 Å; Endsley et al. 2023a). The UV absolute magnitudes range from $M_{\rm UV} = -21$ to -18, similar to typical galaxies at $z \gtrsim 6$ (e.g., Finkelstein et al. 2015; Ishigaki et al. 2018; Bouwens et al. 2021). The UV continuum slopes are fairly blue (median $\beta = -2.2$), signaling modest attenuation from dust. The stellar masses are found to be relatively low (median $= 2.7 \times 10^8\ M_\odot$), and the light-weighted ages are found to be correspondingly young (median 26 Myr). The large [O III]+Hβ EWs in this subset of our sample are primarily driven by large sSFR (median = 40 Gyr^{-1}), signaling a recent upturn in star formation. These properties are all similar to what is seen in most $z \gtrsim 6$ galaxies.

Our spectra reveal a diverse set of Lyα profiles in $z \simeq 2$–3 galaxies with [O III]+Hβ EW = 400–1200 Å. The Lyα EWs range from weak (1 Å) to strong (60 Å) with a median value of 22 Å (see also Du et al. 2020; Tang et al. 2021a). The Lyα velocity offsets also span a wide range, from $v_{\rm peak} = 63$ to 386 km s^{-1} with a median value of 194 km s^{-1} (see examples in Figure 3). In spite of the large sSFR and reasonably low masses, most of these galaxies show very little Lyα emission at the line center (median with $f_{\rm cen,Ly\alpha} = 0.1$), suggesting direct escape of Lyα is not ubiquitous in $z \simeq 2$–3 galaxies with [O III] +Hβ EW = 400–1200 Å. Instead, Lyα photons mostly escape through backscattering and resonant scattering through the

outflowing H I, as is common in most Lyα emitters with lower [O III]+Hβ EWs (e.g., Shapley et al. 2003; Jones et al. 2013; Ouchi et al. 2020). The redshifted component of the Lyα lines is reasonably broad, with an FWHM ranging between 146 and 542 km s^{-1} with a median = 289 km s^{-1}). We occasionally detect Lyα flux redshifted to very high velocities. In five of 11 galaxies with [O III]+Hβ EW = 400–1200 Å and systemic redshift measurements, we detect more than 10% of the line flux redshifted to 500–1000 km s^{-1}. This high-velocity emission is important for visibility in the reionization era, as we will discuss in Section 4.

We detect blue peaks in 18 of the 23 $z \simeq 2$–3 galaxies with [O III]+Hβ EW = 400–1200 Å, reflecting line photons that have resonantly scattered through the near side of the outflowing H I (see Ouchi et al. 2020 for a review). On average, we find 21% of the total Lyα flux is in the blue peak, with typical velocities between −110 and −650 km s^{-1} relative to the line center. We also find 12% of the Lyα flux blueshifted to very high velocities (−1000 to −500 km s^{-1}). The velocity shift of the blue peak is generally larger than that of the red peak, as expected for transfer through outflowing gas (e.g., Verhamme et al. 2006, 2015; Orlitová et al. 2018; Ouchi et al. 2020). In one case (UDS-08964), we see a blue peak ($v_{\rm blue} = -385$ km s^{-1}) that is roughly as strong as the red peak (see Figure 3), with a blue-to-red peak flux ratio of 0.68 ± 0.28. This may reflect transfer through slow-moving H I (e.g., Verhamme et al. 2006, 2015; Li & Gronke 2022), as might be expected if outflows are weak in this galaxy. Regardless of the origin, the blue peak flux fractions are important for interpreting the evolving Lyα EW distribution at $z \gtrsim 6$. As we approach the reionization era, we expect the blue peaks to be strongly attenuated by the IGM (e.g., Hayes et al. 2021), leading to a reduction of Lyα EWs relative to our measurements at $z \simeq 2$–3. We will quantify this in Section 4. The peak separations of the 18 galaxies with [O III]+Hβ EW = 400–1200 Å with double-peak Lyα are large, with a median of $S_{\rm peak} = 571$ km s^{-1}. Together with the negligible $f_{\rm cen,Ly\alpha}$, these indicate that H II regions in most of the [O III] +Hβ EW = 400–1200 Å galaxies are at least partially covered by dense H I (e.g., Verhamme et al. 2015; Li & Gronke 2022).

While most galaxies with [O III]+Hβ EW = 400–1200 Å appear to not have H I conditions that facilitate significant Lyα escape at the line center, we do identify one galaxy in this sample with large Lyα central flux fractions. UDS-11222 ([O III]+Hβ EW = 712 Å, Lyα EW = 48 Å) has a Lyα profile with $f_{\rm cen,Ly\alpha} = 0.39$, more than twice what is typical in this [O III]+Hβ EW range. UDS-11222 stands out as having the lowest stellar mass ($3 \times 10^7\,M_\odot$ for CSFH) and the faintest $M_{\rm UV}$ (−18.3) in the entire $z \simeq 2$–3 sample presented in this paper. The relatively low [O III]+Hβ EW of UDS-11222 (compared to other systems with large Lyα central flux fractions) may be due to a lower metallicity or a more recently declining star formation history at fainter $M_{\rm UV}$ (e.g., Endsley et al. 2023b). SED fitting results also show that UDS-11222 has the largest sSFR (=139 Gyr^{-1}) among those with [O III]+Hβ EW = 400–1200 Å, suggesting it is experiencing a burst of star formation that is more typical of galaxies with [O III]+Hβ EW > 1200 Å. The presence of bursts in low-mass galaxies may help disrupt the neutral gas in galaxies, creating highly ionized channels that allow Lyα to escape directly (e.g., Kimm et al. 2019; Ma et al. 2020). In the next subsection, we explore whether such low-density sightlines are more common in the galaxies in our sample with [O III]+Hβ EW > 1200 Å.

3.3. Lyα Profiles in Galaxies with [O III]+Hβ EW > 1200 Å

We have obtained high-resolution spectra of 13 galaxies with [O III]+Hβ EW > 1200 Å, and all these 13 systems have systemic redshifts necessary for full characterization of the line profiles. The galaxies in this subset are both lower in stellar mass (median $M_\star = 6.5 \times 10^7\,M_\odot$) and larger in sSFR (median = 127 Gyr^{-1}) than those with [O III]+Hβ EW = 400–1200 Å. While our sample is small, the galaxies in this subset have larger Lyα EWs than seen in the rest of the sample (Figure 1). The line profiles are shifted toward lower velocity offsets (median $v_{\rm peak} = 82$ km s^{-1}, with a range of −18–593 km s^{-1}) and larger central flux fractions (median $f_{\rm cen,Ly\alpha} = 0.24$) (see Figure 4). Five of the six galaxies with $f_{\rm cen,Ly\alpha} > 0.38$ (as discussed in Section 3.1) are in the small subsample with [O III]+Hβ EW > 1200 Å. Based on these results, it does seem that the low H I density channels (that are required for line center transmission of Lyα) are more common among the galaxies with the very largest [O III]+Hβ EWs.

However, there are also eight galaxies with extremely strong line emission ([O III]+Hβ EW > 1200 Å) and relatively weak Lyα (6−40 Å) with negligible emission at the line center (median $f_{\rm cen,Ly\alpha} = 0.1$) and large velocity offsets (median $v_{\rm peak} = 230$ km s^{-1}), both suggesting complete coverage of the H II regions with reasonably dense neutral gas (e.g., Erb et al. 2014; Hashimoto et al. 2015; Verhamme et al. 2015). It is conceivable that the weaker Lyα emitters have yet to create the low-density channels necessary for the direct escape of Lyα, perhaps reflecting an earlier evolutionary stage before feedback has disrupted the H I (e.g., Ma et al. 2015; Trebitsch et al. 2017; Barrow et al. 2020). However, there is no evidence from the SEDs that these eight systems (median light-weighted age ≃10 Myr) are younger than the galaxies with Lyα escaping at the line center (median light-weighted age ≃4 Myr). Alternatively, it may just be that some sightlines to galaxies with large sSFR are more likely to be cleared of H I than others. In this case, it is plausible that the dispersion in Lyα profiles at [O III]+Hβ EW > 1200 Å reflects viewing angle effects, with only a subset of sources having low-density sightlines oriented toward us (e.g., Gnedin et al. 2008; Cen & Kimm 2015; Fletcher et al. 2019; Smith et al. 2019; Katz et al. 2020; Nakajima et al. 2020). While such variations are likely to be present in individual galaxies, we have no observations that indicate that this is definitively the case for the systems in our sample.

To better illustrate the physical factors regulating the Lyα profile in our sample, we plot $v_{\rm peak}$ versus sSFR and $f_{\rm cen,Ly\alpha}$ versus sSFR in Figure 6. At large sSFR ($\gtrsim$100 Gyr^{-1}; assuming CSFH) we continue to see high peak velocity offset ($v_{\rm peak} > 200$ km s^{-1}) sources with low central escape factions ($f_{\rm cen,Ly\alpha} < 0.1$). Clearly a recent burst is likely necessary, but not a sufficient criterion for low-density channels that facilitate direct Lyα escape. But in our sample, it is only in this high sSFR sample where we see the low peak velocity offsets ($v_{\rm peak} < 100$ km s^{-1}) and high central escape fraction ($f_{\rm cen,Ly\alpha} > 0.2$) galaxies, indicating lower density sightlines, some of which may be conducive to LyC leakage (e.g., Verhamme et al. 2015; Dijkstra et al. 2016, though with scatter; Pahl et al. 2024). This is consistent with the picture that in high sSFR galaxies, the strong stellar feedback associated with intense bursts can efficiently disrupt the neutral gas

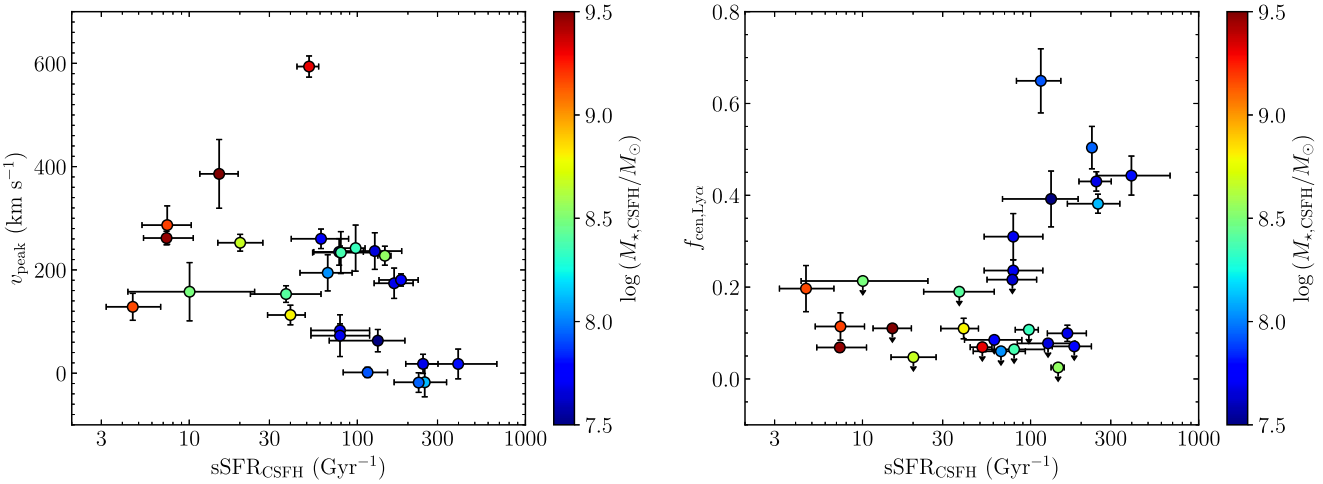

Figure 6. Lyα peak velocity offset (left panel) and Lyα central escape fraction (right panel) as a function of sSFR for our EELGs at $z = 2.1$–3.4. Data are color-coded by stellar mass. Galaxies with very low Lyα peak offsets and large Lyα central escape fractions are low-mass systems ($M_\star \lesssim 10^8\,M_\odot$) with very large sSFRs (>100 Gyr^{-1} assuming CSFH).

surrounding massive stars (e.g., Kimm et al. 2019; Ma et al. 2020; Kakiichi & Gronke 2021). We note that these systems also have low masses, which could imply reduced H I and dust as well (e.g., Erb et al. 2014). Detailed investigations of LyC leakers suggest low-density sightlines may be more common in galaxies with low stellar mass (e.g., Fletcher et al. 2019; Chisholm et al. 2022; Pahl et al. 2023; Saldana-Lopez et al. 2023), whereas trends with sSFR are not as clear (Pahl et al. 2023). It is difficult to distinguish which effect (low mass or large sSFR) is responsible for the low peak velocity offset. It may be that it is the combination of the two factors, i.e., the presence of a burst in a low-mass galaxy, which creates conditions optimal for low peak velocity offset. Larger samples with low masses spanning a larger range of sSFR are required for more insight.

In the following section, we will discuss a sample of $z \gtrsim 7$ galaxies with Lyα emerging at very high velocities (>500 km s^{-1}; Bunker et al. 2023a; Tang et al. 2023; Jung et al. 2024). We find one source in this subset of our sample with a highly redshifted Lyα profile (UDS-08078), similar to the $z \gtrsim 7$ galaxies. In spite of its very large [O III]+Hβ EW (1321 Å), the Lyα escapes with a large peak velocity offset of 593 km s^{-1} and a wide FWHM of 414 km s^{-1}. We find that 45% of the line flux is redshifted to >600 km s^{-1}. The $z \gtrsim 7$ galaxies with large velocity offsets tend to be very luminous. UDS-08078 is similar, with an absolute magnitude ($M_{\rm UV} = -21.7$) that is significantly brighter than the median value in our sample. It is plausible that the most UV-luminous galaxies have larger H I column densities, shifting the emergent Lyα profile to higher velocities (e.g., Mason et al. 2018b; Endsley et al. 2022). This would contribute to the visibility of Lyα in the most luminous galaxies at $z \gtrsim 7$. Larger samples of luminous ($M_{\rm UV} \lesssim -21.5$) EELGs at lower redshifts (where the IGM is highly ionized) are required to determine whether the Lyα velocity offsets are uniformly high in this population.

4. Lyα Profiles in the Reionization Era

4.1. Expectations for Lyα Profiles of EELGs at z > 6

The Lyα line profiles of $z \gtrsim 6$ galaxies are strongly impacted by the IGM, providing a sensitive measure of the local progress of reionization (e.g., Mason & Gronke 2020; Endsley et al. 2022; Saxena et al. 2023; Tang et al. 2024). The utility of line profiles as a probe of the IGM relies on knowledge of the line shape before it is modulated by the IGM. Given their similarity to reionization-era galaxies, the Lyα spectra of $z \simeq 2$–3 EELGs provide a useful baseline for understanding the line profiles now being observed at $z \gtrsim 7$. We have found that the Lyα profiles of $z \simeq 2$–3 EELGs (see Section 2) appear very different from their counterparts at $z \gtrsim 5$ (Tang et al. 2024; see also Section 4.2), with small Lyα peak velocity offsets and often very large central flux fractions. In this subsection, we investigate whether this evolution follows naturally from the impact of the IGM on the centrally peaked EELGs. We will assume that our database of $z \simeq 2$–3 EELG spectra approximates the intrinsic Lyα profile, which we define as the profile emerging from the ISM and CGM. We will first consider the impact of the dense highly ionized IGM at $z \simeq 5$–6, then consider the additional impact of the damping wing as the IGM becomes more neutral at $z \gtrsim 6$.

To explore how the $z \simeq 2$–3 Lyα profiles may appear in the reionization era, we first create a set of composites using the individual spectra obtained in this paper. We include galaxies in our sample with EW$_{\rm [O\,III]+H\beta}$ = 600–3000 Å. This range covers ≃65% of the [O III]+Hβ EWs spanned by $z \simeq 6.5$–8 galaxies (Endsley et al. 2023a), and importantly spans the [O III]+Hβ EWs of most Lyα-emitting galaxies at $z > 7$ (e.g., Finkelstein et al. 2013; Schenker et al. 2014; Oesch et al. 2015; Zitrin et al. 2015; Roberts-Borsani et al. 2016; Stark et al. 2017; Endsley et al. 2021a, 2021b; Larson et al. 2022; Bunker et al. 2023a; Saxena et al. 2023; Tang et al. 2023). We group galaxies by Lyα EW, creating one stack for the strongest Lyα emitters (EW$_{\rm Ly\alpha}$ = 80 Å) and one for moderate Lyα emitters (EW$_{\rm Ly\alpha}$ = 20 Å). To generate the composites, we shift individual spectra to the rest frame using the systemic redshifts. Each spectrum is then interpolated to a common wavelength scale with a bin size (0.125 Å in rest frame) that is larger than the wavelength bin size of individual spectra. We then normalize each individual spectrum using its measured Lyα flux. Finally, the spectra are stacked by median-combining the individual flux densities in each wavelength bin. The composite spectra are shown in Figure 7 as dotted lines, where the rest-frame wavelength is converted to the velocity space. As expected based on the individual profiles (Figure 2), the stack

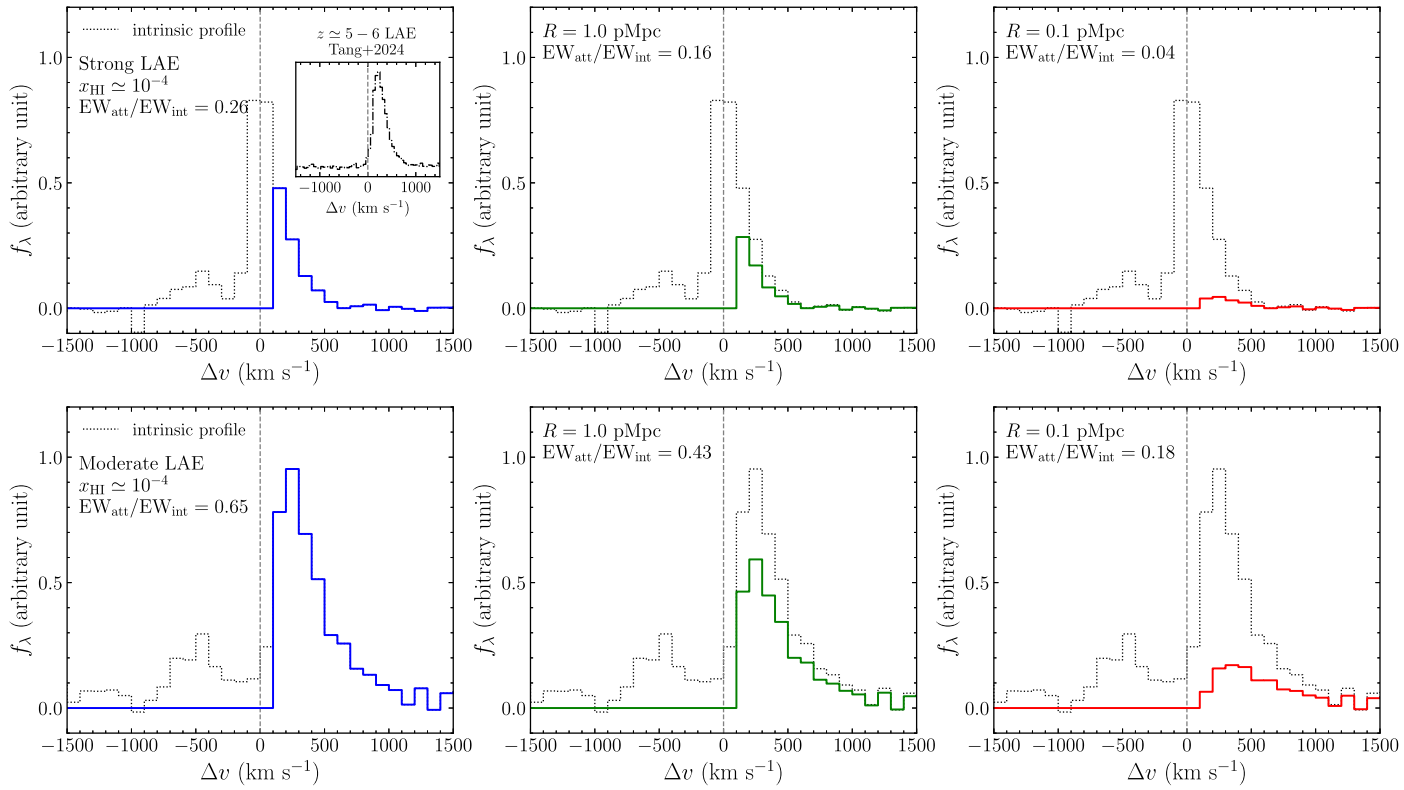

Figure 7. Predicted impact of the IGM attenuation to Lyα profiles of galaxies at $z \gtrsim 6$ (solid color lines). We assume the composite Lyα profile of strong Lyα emitters (EW = 80 Å) of $z = 2.1$–3.4 EELGs as the "intrinsic" profile emerging from the ISM and the CGM (black dotted lines) in top panels and moderate Lyα emitters (EW = 20 Å) in bottom panels. In order to compare with JWST/NIRSpec results, we convolve the profiles with the resolution of NIRSpec grating ($R = 1000$). In left panels, we consider the resonant scattering by the residual H I in the IGM at $z = 6$, which could attenuate the Lyα blueward the line center and the infalling IGM further scatters the Lyα redward. We overplot the composite Lyα profile of $z \simeq 5$–6 galaxies (Tang et al. 2024) as a comparison. In the middle and right panels, we in addition consider the IGM damping wing absorption at $z = 7$. We assume the galaxy is in an ionized bubble, sitting at a distance $R = 1.0$ pMpc (middle panels) or $R = 0.1$ pMpc (right panels) from the neutral IGM. In each panel, we list the fraction of Lyα photons transmitted through the IGM compared to the intrinsic value ($\rm EW_{att}/EW_{int}$).

of the strongest Lyα emitters in our sample has a very large ($f_{\rm cen,Ly\alpha} = 0.47$) with Ly$\alpha$ peaking near the line center. The stack of the more moderate Lyα emitters has a line profile with less emission near systemic ($f_{\rm cen,Ly\alpha} = 0.08$) and the peak velocity occurring at $v_{\rm peak} = 236$ km s^{-1}. We now investigate how these two Lyα profiles would appear at higher redshifts where the IGM is considerably denser and more neutral.

We first consider the impact of the IGM on the composite Lyα profiles at $z \simeq 5$–6. While the IGM is mostly ionized at these redshifts (albeit with non-negligible neutral fractions at $z \simeq 6$), the IGM density is large enough at $z \simeq 5$ for the residual neutral hydrogen ($x_{\rm H\,I} \gtrsim 10^{-5}$–$10^{-4}$; e.g., Yang et al. 2020b; Bosman et al. 2022) to resonantly scatter the blue side of the line (Gunn & Peterson 1965). Given the line profiles we have presented in Section 3, it is clear this will have a significant impact on the recovered fluxes at the tail end of reionization. Considering the two $z \simeq 2$–3 EELG composites described above, we find that the blue side of the line contains 45% and 24% of the total line flux for the strong and moderate Lyα stacks, respectively. This includes emission in the blue peak as well as in the blue half of the central flux component (see Figures 2 and 3). This indicates that the Lyα emission emitted by some EELGs may decrease in EW by up to a factor of 2 due to IGM attenuation between $z \simeq 2$–3 and $z \simeq 5$–6. At $z \simeq 5$–6, the velocity profiles of EELGs should look distinctly different (i.e., sharper blue cutoff) than those of galaxies at $z \simeq 2$–3 with similar Lyα EWs ($\simeq$100 Å). It has been seen that Lyα emitters at $z \simeq 5$–6 generally show negligible flux blueward the line center (Tang et al. 2024), consistent with the strong attenuation to the blue Lyα photons at $z \simeq 5$–6.

Gravitational infall of gas from the IGM onto galaxies is predicted to further alter the line profiles at $z \simeq 5$–6 (e.g., Santos 2004; Dijkstra et al. 2007; Laursen et al. 2011; Mason et al. 2018a), resonantly scattering Lyα photons on the red side of the systemic redshift. This will not only decrease the Lyα EW relative to the $z \simeq 2$–3, but it will shift the peak velocity to the red. To consider the impact of infalling IGM on the $z \simeq 2$–3 EELG line profiles, we adopt the model used in Mason et al. (2018a). Here, gas is assumed to be infalling at the circular velocity of the halo. Halo masses are estimated from redshift and $\rm M_{UV}$ using the abundance matching relations presented in Mason et al. (2015). While more detailed treatments of IGM infall are possible (e.g., Santos 2004; Dijkstra et al. 2007; Sadoun et al. 2017; Weinberger et al. 2018; Park et al. 2021), these are beyond the scope required for the goals in this paper. In the Mason et al. (2018a) model, the impact of infall on the profile will tend to be greater in more luminous galaxies, as the larger halo masses will enable scattering further on the red side of the line. We apply this infall model to our two composite spectra. We adopt an absolute magnitude similar to those of faint galaxies ($M_{\rm UV} = -18$, corresponding to an infall velocity of $\simeq$110 km s^{-1}) now being observed with Lyα at $z \gtrsim 5$ with JWST, but we will comment on how our results would change if we considered more luminous galaxies.

The results are shown in the top left panel of Figure 7 for our strong centrally peaked Lyα composite. As expected, the ionized IGM has a significant effect on the profile given the large fraction of flux near the systemic redshift. For a galaxy with $M_{\rm UV} = -18$, we see that the peak velocity shifts from the line center to 140 km s^{-1} with only 26% of the line transmitted through the IGM. This suggests that the centrally peaked Lyα emitters (which appear commonly in EELG samples at $z \simeq 2$–3) should be somewhat rare at $z \simeq 5$–6 owing to the resonant scattering by the neutral gas in the ionized IGM. This is exactly what is seen (top left panel of Figure 7; see also Tang et al. 2024). The more moderate Lyα emitter stack has a larger peak velocity and hence is less impacted by IGM infall (see the bottom left panel of Figure 7). Again, considering a galaxy with $M_{\rm UV} = -18$, we see that the infall prescription results in a sharper blue cutoff, but the peak velocity (250 km s^{-1}) is not significantly different from the assumed intrinsic profile. Owing to the larger peak velocity of the intrinsic profile, the transmission is less affected by the IGM, with 65% of the line luminosity emerging. As a result, we expect Lyα emitter samples to be increasingly dominated by intrinsic profiles with larger peak velocities at $z \simeq 5$–6.

The Lyα profiles will be further altered at $z \gtrsim 7$, as more of the IGM becomes neutral and the IGM damping wing begins to attenuate the red side of the line in typical galaxies (e.g., Mason et al. 2018a; Hoag et al. 2019; Bolan et al. 2022; Umeda et al. 2023; Nakane et al. 2024). To estimate the impact on the $z \simeq 2$–3 Lyα profiles, we apply the damping wing optical depth of Lyα as a function of velocity offset from systemic (Miralda-Escudé 1998; Dijkstra 2016), while also applying the attenuation due to resonant scattering from the infalling IGM as described above. We consider a galaxy at $z = 7$ situated at the center of an ionized bubble with a distance $R = 1.0$ and 0.1 pMpc from the neutral IGM. For simplicity, as the distance to the first neutral patch of gas dominates the damping wing optical depth (e.g., Mesinger & Furlanetto 2008), we assume the IGM is completely neutral outside the bubble. We again assume a UV-faint galaxy ($M_{\rm UV} = -18$), which minimizes the effect that resonant scattering from infalling IGM gas is likely to have on the lines in the Mason et al. (2018a) models, allowing the effect of the damping wing to be more clearly identified.

The resulting line profiles are shown in the top middle and the top right panels of Figure 7 for the strong Lyα emitter composite. The impact of the IGM damping wing is very pronounced owing to the centrally peaked profile of this composite. For the smallest bubbles considered ($R = 0.1$ pMpc), these simple assumptions suggest the damping wing will only transmit a small fraction ($\simeq$4%) of the line, converting an 80 Å Lyα emitter into a weak 3 Å detection, with the majority of line emission coming out at 100–500 km s^{-1}. For larger ionized regions, the IGM attenuation is still significant, with only 16% of the line emerging in $R = 1.0$ pMpc bubbles. We show the impact of the damping wing on the more moderate Lyα emitter composite in the bottom middle and the bottom right panels of Figure 7. These intrinsic profiles have larger peak velocities and thus face less attenuation, with IGM transmission ranging between 18% and 43% for $R = 0.1$ and 1.0 pMpc bubbles. Such systems should be visible deep in the reionization era, particularly in large ionized regions.

4.2. Lyα Velocity Offsets at z > 6 with JWST

In Section 4.1, we demonstrated that we expect significant evolution in the Lyα profiles of EELGs between $z \simeq 2$–3 and $z \simeq 5$–6, with galaxies having centrally peaked Lyα profiles mostly disappearing from Lyα-selected samples at $z \gtrsim 5$. This has now been shown to occur in Tang et al. (2024), leveraging systemic redshifts from the NIRCam grism in fields with ground-based Lyα detections. In this subsection, we extend the work in Tang et al. (2024) to Lyα peak velocities at $z \gtrsim 6.5$, redshifts where the damping wing may have a stronger effect on the line profiles of sources with detectable Lyα emission. Here, we focus on galaxies with both Lyα detections and systemic redshifts derived from NIRSpec, considering only those systems observed with the medium or high-resolution gratings, as the prism does not give adequate velocity resolution to measure robust line profiles. We are particularly interested in whether galaxies with small peak velocities and large escape fractions can be identified and linked to large ionized bubbles.

Our sample is selected from our own reductions as part of an ongoing effort to build a complete database of Lyα measurements in the reionization era. Our focus in this paper is on galaxies spectroscopically confirmed at $z > 6.5$ using the public JWST/NIRSpec medium-resolution ($R \sim 1000$) or high-resolution ($R \sim 2700$) spectra data set. Full details of this study will be described in a future paper (M. Tang et al. 2024, in preparation), but we will present the full sample with peak velocities in this paper. In brief, we take grating spectra from the following public NIRSpec observations: the JWST Advanced Deep Extragalactic Survey (JADES; Eisenstein et al. 2023a; Bunker et al. 2023b; Eisenstein et al. 2023b), the GLASS-JWST Early Release Science Program (Treu et al. 2022), and the Cosmic Evolution Early Release Science (CEERS. Finkelstein et al. 2024). The JADES NIRSpec observations were performed with the low spectral resolution ($R \sim 100$) PRISM/CLEAR setup and the medium-resolution ($R \sim 1000$) G140M/F070LP and G395M/F290LP grating/filter setups. The GLASS NIRSpec observations were performed with the high-resolution ($R \sim 2700$) G140H/F100LP, G235H/F170LP, and G395H/F290LP grating/filter setups. The CEERS NIRSpec observations were performed with the PRISM/CLEAR and the G140M/F100LP, G235M/F170LP, and G395M/F290LP setups. The NIRSpec spectra used here were reduced by one of the coauthors (M. W. T.) following the procedures described in Tang et al. (2023).

From the above data set, we have identified 75 galaxies at $z > 6.5$ based on detections of rest-frame optical emission lines in medium or high-resolution NIRSpec grating spectra. For these sources, we derive the systemic redshifts by fitting Gaussians to the available strong optical emission lines (Hβ, [O III], or Hα), as in Tang et al. (2023). We then search for Lyα emission lines using the systemic redshifts. Among the 56 galaxies at $z > 6.5$ with NIRSpec grating spectra, we have identified Lyα emission lines in 11 objects. For each object with Lyα emission, we derive the Lyα redshift by fitting the Lyα line with a Gaussian (e.g., JADES-1075; Figure 9) or a truncated Gaussian (e.g., JADES-1899; Figure 8) to account for the impact of the IGM on the blue side of the line. With both Lyα and systemic redshifts, we calculate the Lyα peak velocity offset. To evaluate the uncertainty of Lyα peak velocity offset, we resample the flux densities 1000 times by taking the observed flux densities as mean values and the errors as

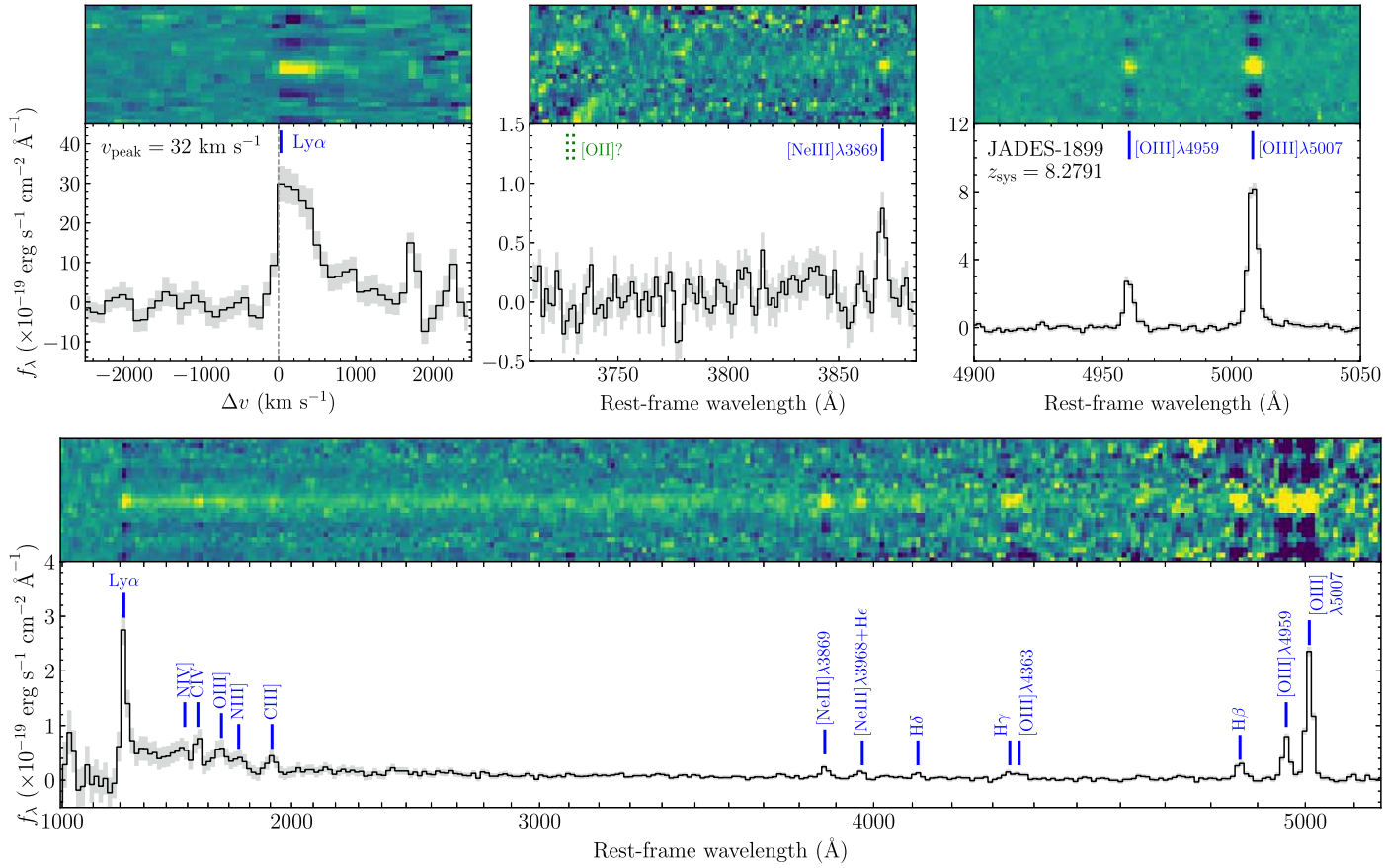

Figure 8. JWST/NIRSpec 2D and 1D medium-resolution ($R \sim 1000$) grating spectrum (top) and low-resolution ($R \sim 100$) prism spectrum (bottom) of the strong Lyα-emitting galaxy at $z = 8.28$ (NIRSpec ID 1899) identified from the public JADES program 1181 data set. More details of this galaxy are presented in Witstok et al. (2024). The top left panel shows the Lyα velocity profile extracted from the G140M/F070LP spectrum. The Lyα peak is close to the systemic redshift (gray dashed line), with a peak velocity offset $v_{\rm peak} = 32 \pm 47$ km s^{-1}. The systemic redshift ($z_{\rm sys} = 8.2791$) used to extract the velocity profile is derived by fitting strong [O III] λ5007 and 4959 emission lines from the G395M/F290LP spectrum (top right). We also find a clear [Ne III] λ3869 detection but we do not detect [O II] $\lambda\lambda$3727, 3729 (top middle), suggesting a very large Ne_3O_2 ratio (>2.6 at 3σ). The prism spectrum (bottom) shows various high-ionization UV emission lines (N IV], C IV, O III], N III], and C III]), indicating a hard ionizing spectrum of this galaxy.

Table 2
Lyα Peak Velocity Offsets of the 11 Galaxies at $z > 6.5$ Derived from Public JWST/NIRSpec Grating ($R \sim 1000$) Spectra

Program	PID	NIRSpec ID	R.A. (hh:mm:ss)	Decl. (dd:mm:ss)	$z_{\rm sys}$	$z_{\rm Ly\alpha}$	$M_{\rm UV}$ (mag)	$v_{\rm peak}$ (km s^{-1})	References
JADES	1181	1899	12:36:47.46	62:15:25.10	8.2791	8.2801	−19.42	32 ± 47	(1, This work)
JADES	1181	1129	12:36:43.16	62:16:56.68	7.0866	7.0899	−19.44	122 ± 53	(This work)
JADES	3215	20213084	03:32:38.14	−27:45:54.25	8.4858	8.4907	−19.47	156 ± 82	(1, 2)
JADES	1181	38420	12:36:42.04	62:16:56.15	6.7332	6.7378	−20.59	178 ± 56	(This work)
JADES	1210	13682	03:32:40.20	−27:46:19.12	7.2754	7.2833	−17.60	217 ± 94	(3, 4)
JADES	1181	1075	12:36:48.63	62:16:31.83	6.9080	6.9140	−19.84	228 ± 55	(This work)
CEERS	1345	1019	14:20:08.49	52:53:26.38	8.6784	8.6877	−22.09	288 ± 161	(5)
CEERS	1345	1027	14:19:31.92	52:50:25.50	7.8188	7.8280	−20.73	313 ± 88	(5)
JADES	1180	8532	03:32:34.93	−27:47:01.85	6.8778	6.8866	−19.86	335 ± 164	(This work)
JADES	1210	9903	03:32:40.56	−27:46:43.65	6.6310	6.6406	−18.63	377 ± 102	(4, This work)
CEERS	1345	698	14:20:12.08	53:00:26.79	7.4703	7.4854	−21.70	535 ± 92	(5)

Note. The systemic redshifts ($z_{\rm sys}$) are derived by fitting strong rest-frame optical emission lines (Hβ, [O III] 4959, [O III] 5007, or Hα) with Gaussian profiles. The Lyα redshifts ($z_{\rm Ly\alpha}$) are derived from the peak of Lyα emission lines. PID: JWST program ID.
References. (1) Witstok et al. (2024); (2) Tang et al. (2024); (3) Saxena et al. (2023); (4) Jones et al. (2024); (5) Tang et al. (2023).

standard deviations. We measure the redshifts and derive the Lyα peak velocity offsets from the resampled spectra and take the standard deviation of $v_{\rm peak}$ as the uncertainty. The derived values of the peak offsets range from 32 to 535 km s^{-1}, with a median $v_{\rm peak} = 228$ km s^{-1} (Table 2). For five sources of the 11 galaxies, the NIRSpec spectra and Lyα detections have previously been reported in the literature (CEERS-698, CEERS-1019, CEERS-1027; Tang et al. 2023; JADES-13682; Saxena et al. 2023; JADES-20213084; Tang et al. 2024; Witstok et al. 2024). In Figures 8 and 9, we show the Lyα velocity profiles of the other

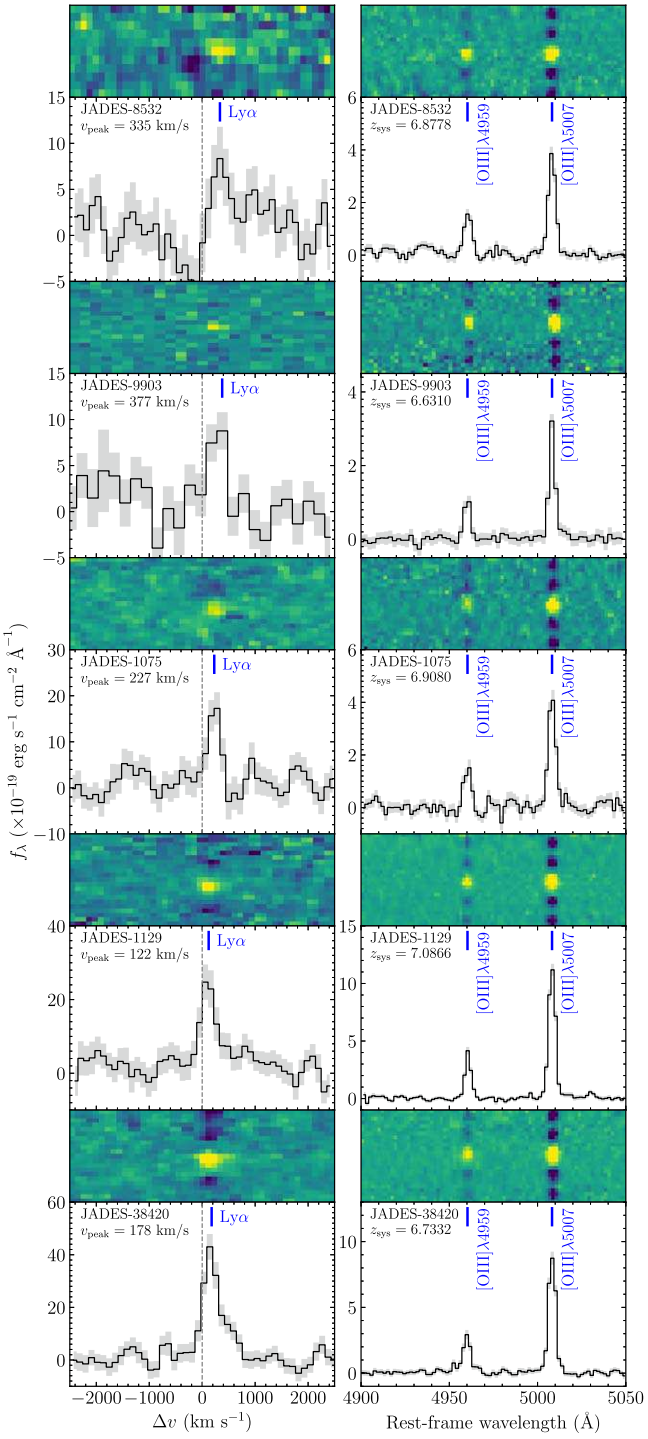

Figure 9. 2D and 1D JWST/NIRSpec medium-resolution ($R \sim 1000$) grating spectra of the five newly discovered Lyα-emitting galaxies at $z > 6.5$ from the public NIRSpec data set (see Table 2, except JADES-1899 shown in Figure 8). For each object we show the Lyα velocity profile on the left and the [O III] λ4959 and 5007 detections on the right. The velocity spaces are converted from the wavelength spaces using the systemic redshifts derived by fitting strong rest-frame optical emission lines with Gaussian profiles.

six newly reported Lyα-emitting galaxies at $z > 6.5$ (we note that the galaxy shown in Figure 8 is also presented in Witstok et al. 2024).

We can now compare the distribution of Lyα profiles at $z \gtrsim 6.5$ to those at $z \simeq 2$–3. In Figure 10 we show the Lyα peak velocity offsets as a function of redshift, limiting our sample to

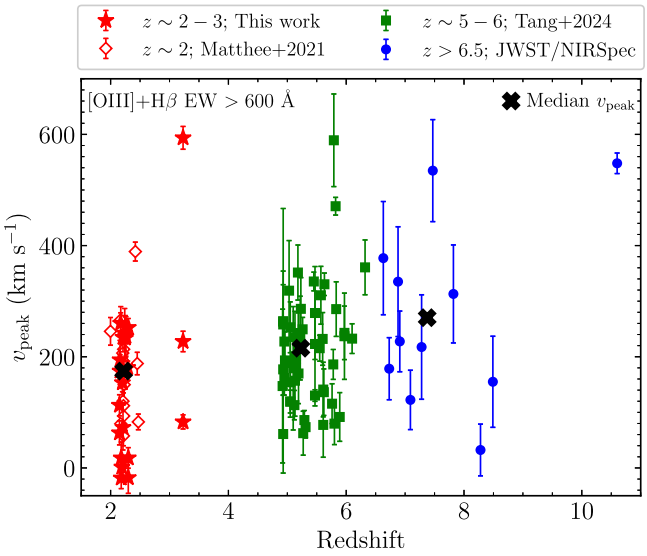

Figure 10. Lyα peak velocity offset evolution for EELGs ([O III]+Hβ EW > 600 Å) over cosmic time. Here, we limit to galaxies with $M_{UV} > -22$. Our $z = 2.1$–3.4 EELGs are shown by filled red stars. We overplot the $z \sim 2$ XLS-z2 sample (Matthee et al. 2021) with open red diamonds. Lyα emitters at $z \simeq 5$–6 are presented by green-filled squares (Tang et al. 2024). We also add Lyα peak velocity offsets of $z > 6.5$ galaxies measured from the publicly available JWST/NIRSpec grating spectra (blue-filled circles; M. Tang et al. 2024, in preparation). We show the median Lyα peak velocity offset of each subsample with black cross symbols.

those with [O III]+Hβ EW > 600 Å. For $z > 6.5$ EELGs with $M_{UV} > -22$, we find that Lyα peak velocity offsets are larger (median $v_{peak} = 230$ km s^{-1}) than those seen in EELGs with strong Lyα emission at $z \simeq 2$–3 (median $v_{peak} = 20$ km s^{-1}). This result naturally follows our discussion in Section 4.1, with the partially neutral IGM at $z > 6.5$ preferentially attenuating the Lyα photons near the line center (Figure 7). As has been described elsewhere (e.g., Endsley et al. 2022; Prieto-Lyon et al. 2023), this will act to weaken Lyα in the galaxies with the smallest velocity offsets, likely shifting the distribution of peak velocities to the subset with Lyα centered at larger redshifts. In Tang et al. (2024), we showed this evolution is already in place at $z \simeq 5$–6. Here, we see a similar trend at yet higher redshifts where the damping wing will play a more prominent role.

4.3. An Intense Lyα-emitting Galaxy at z > 8 with a Small Velocity Offset and Hard Radiation Field

In Tang et al. (2024), we presented a galaxy at $z = 8.49$ with a relatively small velocity offset (156 km s^{-1}) compared to most reionization-era galaxies. Here, we find another $z \gtrsim 8$ galaxy (JADES-1899 at $z = 8.28$) with an even smaller peak velocity, potentially requiring very different surrounding IGM than most $z \gtrsim 8$ galaxies discovered to date. This galaxy is also recently reported in Witstok et al. (2024). In the top of Figure 8, we show the medium-resolution grating spectrum of JADES-1899. Strong [O III] λ4959 and 5007 emission lines are clearly seen in its NIRSpec G395M/F290LP spectrum. By fitting [O III] with Gaussian profiles we derive a systemic redshift of $z_{sys} = 8.2791$. In the G140M/F070LP spectrum, we detect the Lyα emission line with $z_{Ly\alpha} = 8.2801$. This indicates a Lyα peak velocity close to the systemic redshift, with $v_{peak} = 32 \pm 47$ km s^{-1}. The line profile is asymmetric, cutting off sharply at the line center with minimal blue-sided emission. In the remainder of this subsection, we explore the nature of this

source in more detail, with the goal of understanding how such a line profile can exist at $z \gtrsim 8$.

In addition to its unique line profile, JADES-1899 also has one of the strongest Lyα lines yet reported at $z \gtrsim 8$ (see also Fujimoto et al. 2023; Kokorev et al. 2023). We measure a Lyα flux of $F_{\mathrm{Ly}\alpha} = 7.30 \pm 0.52 \times 10^{-18}$ erg s^{-1} cm^{-2} and EW $= 137 \pm 10$ Å. This is well above what has been typically seen to date in $z \gtrsim 8$ star-forming galaxies with JWST (Bunker et al. 2023a; Tang et al. 2023; Jones et al. 2024; Saxena et al. 2024; Tang et al. 2024), where typical sources have EWs that are $10\times$ weaker. We also constrain the Lyα escape fraction using the Hβ emission line. Because the S/N of the Hβ detection in the grating spectrum is low ($\simeq$3), we calculate the Lyα escape fraction using the Lyα and Hβ flux measured from the prism spectrum (bottom panel of Figure 8), which has higher S/N ($\simeq$6). We first correct the Hβ flux for dust attenuation using Balmer decrement measurement. The Hγ/Hβ ratio measured from prism spectrum is 0.474 ± 0.129. Compared to the intrinsic Hγ/Hβ ratio expected in case B recombination (0.468 assuming an electron temperature $T_e = 10^4$ K; Osterbrock & Ferland 2006), this indicates negligible dust attenuation to the nebular emission. Then, assuming case B recombination with $T_e = 10^4$ K and an electron density $n_e = 10^2$ cm^{-3}, we derive a Lyα escape fraction $f_{\mathrm{esc,Ly}\alpha}^{\mathrm{case\ B}} = 0.34 \pm 0.06$. We note that if this galaxy leaks Lyα through optically thin H I gas, case A recombination may be a better approximation. Assuming case A recombination, the Lyα escape fraction is about 1.3 times lower than the value derived from case B recombination, with $f_{\mathrm{esc,Ly}\alpha}^{\mathrm{case\ A}} = 0.26 \pm 0.05$. JADES-1899 appears to be transmitting a much larger fraction of its Lyα than typical systems at $z \gtrsim 8$. At these redshifts, galaxies with detectable Lyα emission are generally found to have very low escape fractions ($f_{\mathrm{esc,Ly}\alpha}^{\mathrm{case\ B}} = 0.03$–$0.09$), consistent with significant damping wing attenuation from the IGM (e.g., Bunker et al. 2023a; Tang et al. 2023).

Both the Lyα escape fraction and line profile in JADES-1899 point to reduced attenuation from the IGM. While this may suggest the galaxy resides in a long ionized sightline (as we will discuss below), it is important to note that this also requires minimal impact from the infalling IGM in the vicinity of the galaxy. As we demonstrated in Figure 7, Lyα profiles are expected to be mostly devoid of emission at $\Delta v = 0$–100 km s^{-1} in cases where infall is important. This is observed in nearly all $z \gtrsim 5$ galaxies (Figure 10). The presence of significant line flux at $\gtrsim$30 km s^{-1} in JADES-1899 requires that the red side of the line center is not resonantly scattered on small scales by infalling gas. We will come back to discuss physical factors that may reduce the impact of infall in JADES-1899 at the end of this subsection.

We also require the effects of the damping wing be small enough for us to recover $\simeq$34% of the Lyα luminosity, consistent with the recovered Lyα escape fraction. To roughly estimate the range of IGM environments that can reproduce the JADES-1899 Lyα profile, we again alter our $z \simeq 2$–3 Lyα profiles following the same methodology applied in Section 4.1. Given the small peak velocity of JADES-1899, we assume that the intrinsic profile is that of our strong Lyα composite shown in top panels of Figure 7 (with significant emission at the line center). We apply the damping wing optical depth of Lyα at $z = 8.28$, assuming the galaxy is in a ionized bubble, sitting a distance $R = 0.5$ or 1.0 pMpc from neutral gas.

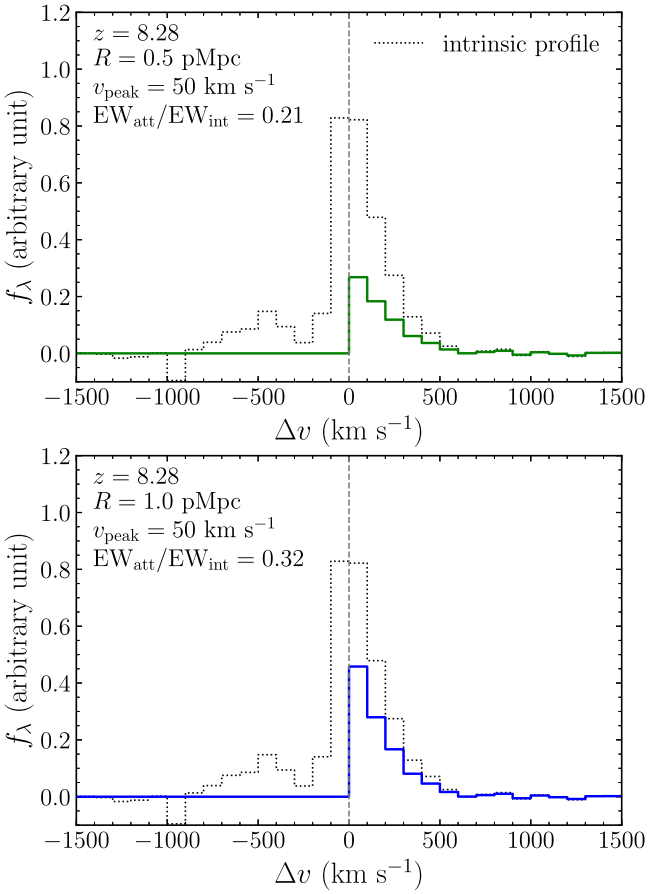

Figure 11. Requirements for observing small Lyα velocity offsets at $z \gtrsim 8$. We assume the composite Lyα profile of strong Lyα emitters of $z = 2.1$–3.4 EELGs as the "intrinsic" profile (black dotted lines). The spectra have been convolved with the resolution of NIRSpec ($R = 1000$). In the top (bottom) panel, we consider the damping wing attenuation assuming the galaxy is centered in an ionized bubble sitting at a distance $R = 0.5$ pMpc ($R = 1.0$ pMpc) from the neutral IGM. To recover the emission near the line center, we must ignore the impact of IGM infall. The Lyα peak velocity is shifted to $v_{\mathrm{peak}} \simeq 50$ km s^{-1}, close to the v_{peak} seen in JADES-1899. The Lyα EW is attenuated by $\simeq$3–5 $\times$ after IGM attenuation (EW$_{\mathrm{att}}$/EW$_{\mathrm{int}} \simeq 0.2$–$0.3$).

We assume that the small residual fraction of neutral hydrogen inside the ionized bubble resonantly scatters the Lyα emission blueward of the line center, but we assume that the effects of IGM infall on the red side of the line are negligible. The results are shown in Figure 11. In a moderate ($R = 0.5$ pMpc; top panel) or large ($R = 1.0$ pMpc; bottom panel) bubble, we find that the Lyα peak velocities have shifted from the line center to values that are consistent with the observed value of JADES-1899 within 1σ uncertainty ($v_{\mathrm{peak}} \simeq 50$ km s^{-1}). The transmission ranges between 21% and 32% in these cases, consistent with the inferred Lyα escape fraction of JADES-1899. We note these calculations suggest that the Lyα profile of JADES-1899 can be explained with a smaller bubble than the $R \sim 3$ pMpc bubble size predicted in the analysis of Witstok et al. (2024). While these calculations are mostly meant as illustrative of the possible range of bubbles that might host JADES-1899 ($R \gtrsim 0.5$–1 pMpc), it is clear that much smaller bubbles (e.g., $R = 0.1$ pMpc) would result in stronger attenuation just redward of the line center. In this case, the peak velocities would be shifted to larger values ($\simeq$250 km s^{-1}) and would give an escape fraction ($\simeq$4%) that is much smaller than observed.

The IGM conditions that give rise to the Lyα profile of JADES-1899 must be rare at $z \gtrsim 8$. On one hand, this may suggest that the moderate-size bubbles ($\gtrsim$0.5–1 pMpc) required to explain the transmission are not common at $z \gtrsim 8$, as would be expected at very early stages of reionization when neutral fractions are very large ($x_{\rm H\,I} \simeq 0.9$; Lu et al. 2024). But the absence of significant attenuation from infalling IGM may also reflect unique conditions on smaller scales. For example, a hard radiation field could decrease the residual H I fraction in the ionized IGM surrounding JADES-1899, reducing the impact of resonant scattering on the line profile (Mason & Gronke 2020) or we may be observing Lyα escaping along a sightline without significant infall. Simulations predict a broad distribution of infall velocities whereby complex gas dynamics and strong outflows can counteract the spherical infall of IGM gas (e.g., Iliev et al. 2008; Muratov et al. 2015; Park et al. 2021). The spectrum of JADES-1899 is consistent with this picture, revealing a suite of intense rest-frame UV and optical emission lines seen in only a handful of early galaxies (Figure 8). In particular, we detect high ionization UV emission lines in the prism spectrum (Figure 8). The most prominent line is C IV $\lambda\lambda$1548, 1551, with unresolved doublet EW $=49 \pm 16$ Å. Such large EW C IV emission is extremely rare at lower redshifts (Senchyna et al. 2017; Berg et al. 2019; Izotov et al. 2024) but is present in a small subset of reionization-era galaxies with metal-poor gas (e.g., Stark et al. 2015; Castellano et al. 2024; Topping et al. 2024). We also find tentative detections (S/N $\simeq 2$) of blended He II λ1640+O III] $\lambda\lambda$1661, 1666 (EW $= 65 \pm 25$ Å), C III] $\lambda\lambda$1907, 1909 (EW $= 50 \pm 22$ Å), and nitrogen emission lines N IV] $\lambda\lambda$1483, 1486 (EW $= 35 \pm 20$ Å) and N III] $\lambda\lambda$1746, 1748 (EW $=35 \pm 22$ Å). The rest-frame optical presents a similar picture, with an intense [O III] emission ([O III] λ5007 EW $=1625 \pm 113$ Å) and an extremely large ionization-sensitive line ratio ([O III]/[O II] > 40). We may thus be observing JADES-1899 at a special time when its hard radiation field is facilitating enhanced transmission of Lyα near the line center, while a relatively long ionized sightline is simultaneously reducing the impact of the damping wing on Lyα.

5. Summary

We have presented resolved ($R \simeq 3900$) Lyα profiles of 42 extreme [O III] line-emitting galaxies at $z = 2.1$–3.4, which have [O III]+Hβ EWs ($\simeq$300–3000 Å) that are similar to the range seen in reionization-era systems (e.g., De Barros et al. 2019; Endsley et al. 2021b, 2023a). Twenty-six of the 42 sources in our sample have systemic redshift measurements, enabling us to derive their detailed Lyα profile properties. We use these to investigate the neutral hydrogen distribution in the ISM and the CGM of galaxies with properties similar to those of the reionization era. Using our database of Lyα spectra, we consider how the IGM is likely to modify the Lyα profiles at $z \gtrsim 6$. Below we summarize our findings.

1. We have identified six sources with extremely large Lyα central escape fraction ($f_{\rm cen,Ly\alpha} \gtrsim 0.4$) in our sample, indicating that EELGs occasionally create very low-density H I channels allowing direct escape of Lyα photons. These galaxies have the largest [O III]+Hβ EWs (median $\simeq$1900 Å) and the largest Lyα EWs (median $z \simeq 90$ Å) among objects in our sample. SED fitting indicates that the light of these six large $f_{\rm cen,Ly\alpha}$ systems is dominated by extremely young populations (2–8 Myr assuming CSFH) with very large sSFRs (115–400 Gyr^{-1}) and low-stellar masses (3×10^7–$1 \times 10^8\,M_\odot$), suggesting that low-density H I channels can form in low-mass systems undergoing intense bursts of star formation. Those galaxies with large central flux fractions are often seen with a red tail of Lyα emission (extending to 300–400 km s^{-1}) and a blue peak, potentially indicating that the very low-density H I gas is surrounded by denser H I which scatters Lyα to larger velocities.
2. Galaxies with [O III]+Hβ EWs (=400–1200 Å) that are typical of the range seen in the reionization era (median EW = 780 Å; e.g., Endsley et al. 2023a) present a range of Lyα profiles. Most exhibit moderate strength Lyα (median EW = 22 Å) with large Lyα peak velocity offsets (median $v_{\rm peak} = 193$ km s^{-1}) and small Lyα central escape fractions (median $f_{\rm cen,Ly\alpha} = 0.1$), consistent with the standard expectations from backscattering and resonant scattering through the outflowing H I. This indicates that EELGs often lack the low-density H I channels required for direct escape of Lyα. Due to the dense H I in the ISM or the CGM, Lyα flux in these systems is often scattered to very high velocities of 500–1000 km s^{-1}. About 21% (on average) of the Lyα flux of [O III]+Hβ EW = 400–1200 Å galaxies in our sample is in blue peak Lyα with velocity $= -650$ to -110 km s^{-1}.
3. Our sample contains 13 galaxies with the largest [O III]+Hβ EWs (>1200 Å). This population is rare at $z \simeq 2$–3 but becomes more common at $z > 6$. These systems are characterized by both low stellar masses (median $= 6.5 \times 10^7\,M_\odot$) and very large sSFRs (median $= 127$ Gyr^{-1}). Five of these 13 galaxies present large $f_{\rm cen,Ly\alpha}$ ($\gtrsim$0.4) and low $v_{\rm peak}$ (<100 km s^{-1}), indicating low-density sightlines, which may be conducive to LyC leakage. On the other hand, the other eight galaxies with [O III]+Hβ EW > 1200 Å in our sample show relatively weak Lyα EWs (=6–40 Å) with larger $v_{\rm peak}$ (median = 230 km s^{-1}) and negligible Lyα flux near the line center (median $f_{\rm cen,Ly\alpha} = 0.1$). These suggest more uniformly covered dense H I gas surrounding H II regions. The most UV-luminous ($M_{\rm UV} = -21.5$) galaxy in our sample shows the largest $v_{\rm peak}$ (=593 km s^{-1}) with a wide FWHM (=414 km s^{-1}). It is possible that such luminous galaxies have denser H I columns that scatter Lyα to higher velocities, though Lyα spectroscopy of a larger sample of luminous EELGs ($M_{\rm UV} < -21.5$) at redshifts where the IGM is highly ionized is required to examine this scenario.
4. Assuming the Lyα profiles in our $z \simeq 2$–3 sample are similar to those emerging from $z \gtrsim 6$ galaxies, we explore how the profiles will be modulated by the IGM in the reionization era. At $z \simeq 5$–6, the Lyα flux blueward the systemic redshift will likely be highly attenuated due to the residual H I in high density IGM (i.e., the Gunn-Peterson effect). The infall of IGM at $z \simeq 5$–6 could further scatter the Lyα redward the systemic redshift, shifting the Lyα peak to 140–250 km s^{-1} in galaxies with $M_{\rm UV} = -18$. We also consider the impact of the neutral IGM on the $z \simeq 2$–3 Lyα profiles at $z \gtrsim 7$ in $R = 0.1$ and 1.0 pMpc ionized bubbles. The IGM damping wing together with the infall of IGM will highly attenuate the

subset of EELGs with strong centrally peaked Lyα emission, transmitting only 4% ($R = 0.1$ pMpc) to 16% ($R = 1.0$ pMpc) of the line radiation. In many EELGs in our sample, Lyα emerges with a larger peak velocity ($\simeq$250–350 km s^{-1}), allowing a greater fraction (18%–43%) of the line to be transmitted through the damping wing of the neutral IGM. Our results suggest that the reionization-era IGM will lead to a disappearance of the centrally peaked Lyα emitters, which appear commonly in $z \simeq 2$–3 EELG samples. This picture is consistent with $z > 5$ Lyα detections (Tang et al. 2024).

5. We present the Lyα peak velocity offsets of 11 galaxies at $z > 6.5$ derived from the public JWST/NIRSpec data set. At fixed M_{UV} and [O III]+Hβ EW, galaxies at $z > 6.5$ show much larger Lyα peak offsets (median $v_{peak} = 230$ km s^{-1}) than the strong Lyα emitters at $z \simeq 2$–3 (median $v_{peak} = 20$ km s^{-1}), reflecting the partially neutral IGM at $z > 6.5$ preferentially attenuating the Lyα near the systemic redshift. We report a new Lyα emitter at $z = 8.3$ identified from the JADES program 1181. This object is also presented in Witstok et al. (2024). We measure its Lyα emission with a very large EW = 137 Å and a low peak velocity offset $v_{peak} = 32$ km s^{-1}. The low peak velocity offset and the relatively large Lyα escape fraction ($f_{esc,Ly\alpha}^{case\ B} = 0.34$) suggest that this galaxy is likely to be situated in a fairly long ($\gtrsim$0.5–1.0 pMpc) ionized sightline at $z = 8.3$. Detecting such low peak velocity offset also implies negligible resonant scattering by residual neutral gas infalling onto the galaxy. We also identify intense high ionization UV emission lines (C IV, N IV]) in this object, potentially indicating a hard radiation field, which could reduce the local residual neutral gas fraction.

Acknowledgments

The authors acknowledge the anonymous referee for the insightful comments, which improved the manuscript. We thank Joris Witstok for useful discussions and Jorryt Matthee for kindly sharing data of the X-SHOOTER Lyman α survey at $z = 2$ (XLS-z2; Matthee et al. 2021). We also thank Stéphane Charlot and Jacopo Chevallard for providing access to the BEAGLE tool used for SED fitting analysis. M.T. acknowledges funding from the JWST Arizona/Steward Postdoc in Early galaxies and Reionization (JASPER) Scholar contract at the University of Arizona. M.T. and R.S.E. also acknowledge funding from the European Research Council under the European Union Horizon 2020 research and innovation program (grant agreement No. 669253). D.P.S. acknowledges support from the National Science Foundation through the grant AST-2109066. C.A.M. acknowledges support by the VILLUM FONDEN under grant 37459 and the Carlsberg Foundation under grant CF22-1322. The Cosmic Dawn Center (DAWN) is funded by the Danish National Research Foundation under grant DNRF140. Z.L. has been supported in part by grant AST-2009278 from the U.S. National Science Foundation.

The Binospec spectra used in this paper were obtained at the MMT Observatory, a joint facility of the University of Arizona and the Smithsonian Institution. We acknowledge the MMT queue observers for assisting with MMT/Binospec observations. The HST imaging and grism spectra used in this work are based on observations taken by the 3D-HST Treasury Program (GO 12177 and 12328) with the NASA/ESA Hubble Space Telescope obtained from the Space Telescope Science Institute (STScI), which is operated by the Association of Universities for Research in Astronomy, Inc., under NASA contract NAS 5-26555. This research is based in part on observations made with the NASA/ESA/CSA James Webb Space Telescope from the STScI under NASA contract NAS 5-03127. These observations are associated with program Nos. 1180, 1181, 1210, 1345, and 3215. The JWST data were obtained from the Mikulski Archive for Space Telescopes at the STScI.

Facilities: MMT (Binospec), HST (ACS and WFC3), JWST (NIRSpec).

Software: `NumPy` (Harris et al. 2020), `matplotlib` (Hunter 2007), `SciPy` (Virtanen et al. 2020), `astropy` (Astropy Collaboration et al. 2013), `BEAGLE` (Chevallard & Charlot 2016), `Cloudy` (Ferland et al. 2013)

Data Availability

The HST and JWST data used in this work can be found in the Mikulski Archive for Space Telescopes (https://mast.stsci.edu/): Momcheva (2017); Rieke et al. (2023) and Finkelstein et al. (2023). Other data underlying this article will be shared on reasonable request to the corresponding author.

ORCID iDs

Mengtao Tang https://orcid.org/0000-0001-5940-338X
Richard S. Ellis https://orcid.org/0000-0001-7782-7071
Charlotte Mason https://orcid.org/0000-0002-3407-1785
Zhihui Li https://orcid.org/0000-0001-5113-7558

References

Almada Monter, S., & Gronke, M. 2024, MNRAS, 534, L7
Astropy Collaboration, Robitaille, T. P., Tollerud, E. J., et al. 2013, A&A, 558, A33
Bañados, E., Venemans, B. P., Mazzucchelli, C., et al. 2018, Natur, 553, 473
Barrow, K. S. S., Robertson, B. E., Ellis, R. S., et al. 2020, ApJL, 902, L39
Behrens, C., Dijkstra, M., & Niemeyer, J. C. 2014, A&A, 563, A77
Berg, D. A., Chisholm, J., Erb, D. K., et al. 2019, ApJL, 878, L3
Bolan, P., Lemaux, B. C., Mason, C., et al. 2022, MNRAS, 517, 3263
Bosman, S. E. I., Ďurovčíková, D., Davies, F. B., & Eilers, A.-C. 2021, MNRAS, 503, 2077
Bosman, S. E. I., Davies, F. B., Becker, G. D., et al. 2022, MNRAS, 514, 55
Bouwens, R. J., Oesch, P. A., Stefanon, M., et al. 2021, AJ, 162, 47
Bouwens, R. J., Stefanon, M., Brammer, G., et al. 2023, MNRAS, 523, 1036
Boyett, K., Bunker, A. J., Curtis-Lake, E., et al. 2024, arXiv:2401.16934
Boyett, K. N. K., Stark, D. P., Bunker, A. J., Tang, M., & Maseda, M. V. 2022, MNRAS, 513, 4451
Bruzual, G., & Charlot, S. 2003, MNRAS, 344, 1000
Bunker, A. J., Saxena, A., Cameron, A. J., et al. 2023a, A&A, 677, A88
Bunker, A. J., Cameron, A. J., Curtis-Lake, E., et al. 2023b, arXiv:2306.02467
Calzetti, D., Kinney, A. L., & Storchi-Bergmann, T. 1994, ApJ, 429, 582
Caruana, J., Bunker, A. J., Wilkins, S. M., et al. 2014, MNRAS, 443, 2831
Castellano, M., Dayal, P., Pentericci, L., et al. 2016, ApJL, 818, L3
Castellano, M., Napolitano, L., Fontana, A., et al. 2024, arXiv:2403.10238
Cen, R., & Kimm, T. 2015, ApJL, 801, L25
Chen, Z., Stark, D. P., Mason, C., et al. 2024, MNRAS, 528, 7052
Chevallard, J., & Charlot, S. 2016, MNRAS, 462, 1415
Chevallard, J., Charlot, S., Senchyna, P., et al. 2018, MNRAS, 479, 3264
Chisholm, J., Saldana-Lopez, A., Flury, S., et al. 2022, MNRAS, 517, 5104
Choustikov, N., Katz, H., Saxena, A., et al. 2024, MNRAS, 532, 2463
Cooper, O. R., Casey, C. M., Akins, H. B., et al. 2024, ApJ, 970, 50
Davies, F. B., Hennawi, J. F., Bañados, E., et al. 2018, ApJ, 864, 142
Dayal, P., Ferrara, A., Saro, A., et al. 2009, MNRAS, 400, 2000
De Barros, S., Oesch, P. A., Labbé, I., et al. 2019, MNRAS, 489, 2355
Dijkstra, M. 2014, PASA, 31, e040

Dijkstra, M. 2016, in Understanding the Epoch of Cosmic Reionization: Challenges and Progress, ed. A. Mesinger, Vol. 423 (Berlin: Springer), 145
Dijkstra, M., Gronke, M., & Venkatesan, A. 2016, ApJ, 828, 71
Dijkstra, M., Lidz, A., & Wyithe, J. S. B. 2007, MNRAS, 377, 1175
Du, X., Shapley, A. E., Tang, M., et al. 2020, ApJ, 890, 65
Eisenstein, D. J., Willott, C., Alberts, S., et al. 2023a, arXiv:2306.02465
Eisenstein, D. J., Johnson, B. D., Robertson, B., et al. 2023b, arXiv:2310.12340
Endsley, R., & Stark, D. P. 2022, MNRAS, 511, 6042
Endsley, R., Stark, D. P., Charlot, S., et al. 2021a, MNRAS, 502, 6044
Endsley, R., Stark, D. P., Chevallard, J., & Charlot, S. 2021b, MNRAS, 500, 5229
Endsley, R., Stark, D. P., Whitler, L., et al. 2023a, MNRAS, 524, 2312
Endsley, R., Stark, D. P., Bouwens, R. J., et al. 2022, MNRAS, 517, 5642
Endsley, R., Stark, D. P., Whitler, L., et al. 2023b, arXiv:2306.05295
Erb, D. K., Steidel, C. C., Trainor, R. F., et al. 2014, ApJ, 795, 33
Fabricant, D., Fata, R., Epps, H., et al. 2019, PASP, 131, 075004
Fan, X., Bañados, E., & Simcoe, R. A. 2023, ARA&A, 61, 373
Ferland, G. J., Porter, R. L., van Hoof, P. A. M., et al. 2013, RMxAA, 49, 137
Finkelstein, S., Bagley, M., & Yang, G. 2023, Data from The Cosmic Evolution Early Release Science Survey (CEERS), MAST, doi:10.17909/z7p0-8481
Finkelstein, S. L., Leung, G. C. K., Bagley, M. B., et al. 2024, ApJL, 969, L2
Finkelstein, S. L., Papovich, C., Dickinson, M., et al. 2013, Natur, 502, 524
Finkelstein, S. L., Ryan, R. E. J., Papovich, C., et al. 2015, ApJ, 810, 71
Fletcher, T. J., Tang, M., Robertson, B. E., et al. 2019, ApJ, 878, 87
Flury, S. R., Jaskot, A. E., Ferguson, H. C., et al. 2022, ApJ, 930, 126
Fujimoto, S., Wang, B., Weaver, J., et al. 2023, arXiv:2308.11609
Gardner, J. P., Mather, J. C., Abbott, R., et al. 2023, PASP, 135, 068001
Gazagnes, S., Chisholm, J., Schaerer, D., Verhamme, A., & Izotov, Y. 2020, A&A, 639, A85
Gnedin, N. Y., Kravtsov, A. V., & Chen, H.-W. 2008, ApJ, 672, 765
Goto, H., Shimasaku, K., Yamanaka, S., et al. 2021, ApJ, 923, 229
Greig, B., Mesinger, A., Davies, F. B., et al. 2022, MNRAS, 512, 5390
Grogin, N. A., Kocevski, D. D., Faber, S. M., et al. 2011, ApJS, 197, 35
Gunn, J. E., & Peterson, B. A. 1965, ApJ, 142, 1633
Gutkin, J., Charlot, S., & Bruzual, G. 2016, MNRAS, 462, 1757
Harris, C. R., Millman, K. J., van der Walt, S. J., et al. 2020, Natur, 585, 357
Hashimoto, T., Verhamme, A., Ouchi, M., et al. 2015, ApJ, 812, 157
Hayes, M., Östlin, G., Schaerer, D., et al. 2010, Natur, 464, 562
Hayes, M. J., Runnholm, A., Gronke, M., & Scarlata, C. 2021, ApJ, 908, 36
Hayes, M. J., & Scarlata, C. 2023, ApJL, 954, L14
Henry, A., Scarlata, C., Martin, C. L., & Erb, D. 2015, ApJ, 809, 19
Hoag, A., Bradač, M., Huang, K., et al. 2019, ApJ, 878, 12
Hu, W., Martin, C. L., Gronke, M., et al. 2023, ApJ, 956, 39
Hunter, J. D. 2007, CSE, 9, 90
Iliev, I. T., Shapiro, P. R., McDonald, P., Mellema, G., & Pen, U.-L. 2008, MNRAS, 391, 63
Ishigaki, M., Kawamata, R., Ouchi, M., et al. 2018, ApJ, 854, 73
Itoh, R., Ouchi, M., Zhang, H., et al. 2018, ApJ, 867, 46
Izotov, Y. I., Schaerer, D., Guseva, N. G., Thuan, T. X., & Worseck, G. 2024, MNRAS, 528, L10
Izotov, Y. I., Worseck, G., Schaerer, D., et al. 2021, MNRAS, 503, 1734
Izotov, Y. I., Worseck, G., Schaerer, D., et al. 2018, MNRAS, 478, 4851
Jakobsen, P., Ferruit, P., Alves de Oliveira, C., et al. 2022, A&A, 661, A80
Jaskot, A. E., Dowd, T., Oey, M. S., Scarlata, C., & McKinney, J. 2019, ApJ, 885, 96
Jin, X., Yang, J., Fan, X., et al. 2023, ApJ, 942, 59
Jones, G. C., Bunker, A. J., Saxena, A., et al. 2024, A&A, 683, A238
Jones, T. A., Ellis, R. S., Schenker, M. A., & Stark, D. P. 2013, ApJ, 779, 52
Jung, I., Finkelstein, S. L., Larson, R. L., et al. 2022, arXiv:2212.09850
Jung, I., Finkelstein, S. L., Arrabal Haro, P., et al. 2024, ApJ, 967, 73
Kakiichi, K., & Gronke, M. 2021, ApJ, 908, 30
Kansky, J., Chilingarian, I., Fabricant, D., et al., 2019 Binospec: Data reduction pipeline for the Binospec imaging spectrograph, Astrophysics Source Code Library, ascl:1905.004
Katz, H., Ďurovčíková, D., Kimm, T., et al. 2020, MNRAS, 498, 164
Kimm, T., Blaizot, J., Garel, T., et al. 2019, MNRAS, 486, 2215
Koekemoer, A. M., Faber, S. M., Ferguson, H. C., et al. 2011, ApJS, 197, 36
Kokorev, V., Fujimoto, S., Labbe, I., et al. 2023, ApJL, 957, L7
Konno, A., Ouchi, M., Shibuya, T., et al. 2018, PASJ, 70, S16
Kornei, K. A., Shapley, A. E., Erb, D. K., et al. 2010, ApJ, 711, 693
Kriek, M., Shapley, A. E., Reddy, N. A., et al. 2015, ApJS, 218, 15
Labbé, I., Oesch, P. A., Bouwens, R. J., et al. 2013, ApJL, 777, L19
Larson, R. L., Finkelstein, S. L., Hutchison, T. A., et al. 2022, ApJ, 930, 104
Laursen, P., Sommer-Larsen, J., & Razoumov, A. O. 2011, ApJ, 728, 52
Leonova, E., Oesch, P. A., Qin, Y., et al. 2022, MNRAS, 515, 5790
Li, Z., & Gronke, M. 2022, MNRAS, 513, 5034
Li, Z., Steidel, C. C., Gronke, M., & Chen, Y. 2021, MNRAS, 502, 2389
Lu, T.-Y., Mason, C. A., Hutter, A., et al. 2024, MNRAS, 528, 4872
Lujan Niemeyer, M., Bowman, W. P., Ciardullo, R., et al. 2022, ApJL, 934, L26
Ma, X., Kasen, D., Hopkins, P. F., et al. 2015, MNRAS, 453, 960
Ma, X., Quataert, E., Wetzel, A., et al. 2020, MNRAS, 498, 2001
Mármol-Queraltó, E., McLure, R. J., Cullen, F., et al. 2016, MNRAS, 460, 3587
Maseda, M. V., van der Wel, A., Rix, H.-W., et al. 2014, ApJ, 791, 17
Mason, C. A., & Gronke, M. 2020, MNRAS, 499, 1395
Mason, C. A., Trenti, M., & Treu, T. 2015, ApJ, 813, 21
Mason, C. A., Treu, T., Dijkstra, M., et al. 2018a, ApJ, 856, 2
Mason, C. A., Treu, T., de Barros, S., et al. 2018b, ApJL, 857, L11
Mason, C. A., Fontana, A., Treu, T., et al. 2019, MNRAS, 485, 3947
Matthee, J., Sobral, D., Best, P., et al. 2017, MNRAS, 465, 3637
Matthee, J., Sobral, D., Oteo, I., et al. 2016, MNRAS, 458, 449
Matthee, J., Sobral, D., Hayes, M., et al. 2021, MNRAS, 505, 1382
McGreer, I. D., Mesinger, A., & D'Odorico, V. 2015, MNRAS, 447, 499
McQuinn, M., Hernquist, L., Zaldarriaga, M., & Dutta, S. 2007, MNRAS, 381, 75
Mesinger, A., Aykutalp, A., Vanzella, E., et al. 2015, MNRAS, 446, 566
Mesinger, A., & Furlanetto, S. R. 2008, MNRAS, 385, 1348
Mesinger, A., Haiman, Z., & Cen, R. 2004, ApJ, 613, 23
Miralda-Escudé, J. 1998, ApJ, 501, 15
Momcheva, I. 2017, 3D-HST, MAST, doi:10.17909/T9JW9Z
Momcheva, I. G., Brammer, G. B., van Dokkum, P. G., et al. 2016, ApJS, 225, 27
Muratov, A. L., Kereš, D., Faucher-Giguère, C.-A., et al. 2015, MNRAS, 454, 2691
Naidu, R. P., Oesch, P. A., Reddy, N., et al. 2017, ApJ, 847, 12
Naidu, R. P., Matthee, J., Oesch, P. A., et al. 2022, MNRAS, 510, 4582
Nakajima, K., Ellis, R. S., Robertson, B. E., Tang, M., & Stark, D. P. 2020, ApJ, 889, 161
Nakane, M., Ouchi, M., Nakajima, K., et al. 2024, ApJ, 967, 28
Napolitano, L., Pentericci, L., Santini, P., et al. 2024, arXiv:2402.11220
Ning, Y., Cai, Z., Jiang, L., et al. 2023, ApJL, 944, L1
Oesch, P. A., van Dokkum, P. G., Illingworth, G. D., et al. 2015, ApJL, 804, L30
Oke, J. B., & Gunn, J. E. 1983, ApJ, 266, 713
Orlitová, I., Verhamme, A., Henry, A., et al. 2018, A&A, 616, A60
Osterbrock, D. E., & Ferland, G. J. 2006, Astrophysics of Gaseous Nebulae and Active Galactic Nuclei (Mill Valley, CA: Univ. Science Books)
Ota, K., Iye, M., Kashikawa, N., et al. 2017, ApJ, 844, 85
Ouchi, M., Ono, Y., & Shibuya, T. 2020, ARA&A, 58, 617
Ouchi, M., Shimasaku, K., Furusawa, H., et al. 2010, ApJ, 723, 869
Pahl, A. J., Shapley, A., Steidel, C. C., et al. 2023, MNRAS, 521, 3247
Pahl, A. J., Shapley, A. E., Steidel, C. C., et al. 2024, arXiv:2401.09526
Park, H., Jung, I., Song, H., et al. 2021, ApJ, 922, 263
Pentericci, L., Vanzella, E., Castellano, M., et al. 2018, A&A, 619, A147
Planck Collaboration, Aghanim, N., Akrami, Y., et al. 2020, A&A, 641, A6
Prieto-Lyon, G., Mason, C., Mascia, S., et al. 2023, ApJ, 956, 136
Qin, Y., Wyithe, J. S. B., Oesch, P. A., et al. 2022, MNRAS, 510, 3858
Reddy, N., Dickinson, M., Elbaz, D., et al. 2012, ApJ, 744, 154
Rieke, M., Robertson, B., Tacchella, S., et al. 2023, Data from the JWST Advanced Deep Extragalactic Survey (JADES), MAST, doi:10.17909/8tdj-8n28
Rivera-Thorsen, T. E., Dahle, H., Gronke, M., et al. 2017, A&A, 608, L4
Rivera-Thorsen, T. E., Dahle, H., Chisholm, J., et al. 2019, Sci, 366, 738
Roberts-Borsani, G. W., Bouwens, R. J., Oesch, P. A., et al. 2016, ApJ, 823, 143
Robertson, B. E. 2022, ARA&A, 60, 121
Sadoun, R., Zheng, Z., & Miralda-Escudé, J. 2017, ApJ, 839, 44
Saldana-Lopez, A., Schaerer, D., Chisholm, J., et al. 2023, MNRAS, 522, 6295
Santini, P., Fontana, A., Castellano, M., et al. 2017, ApJ, 847, 76
Santos, M. R. 2004, MNRAS, 349, 1137
Saxena, A., Robertson, B. E., Bunker, A. J., et al. 2023, A&A, 678, A68
Saxena, A., Bunker, A. J., Jones, G. C., et al. 2024, A&A, 684, A84
Schenker, M. A., Ellis, R. S., Konidaris, N. P., & Stark, D. P. 2014, ApJ, 795, 20
Senchyna, P., Stark, D. P., Vidal-García, A., et al. 2017, MNRAS, 472, 2608
Shapley, A. E., Steidel, C. C., Pettini, M., & Adelberger, K. L. 2003, ApJ, 588, 65
Shivaei, I., Reddy, N. A., Siana, B., et al. 2018, ApJ, 855, 42
Simmonds, C., Tacchella, S., Maseda, M., et al. 2023, MNRAS, 523, 5468

Skelton, R. E., Whitaker, K. E., Momcheva, I. G., et al. 2014, ApJS, 214, 24
Smit, R., Bouwens, R. J., Labbé, I., et al. 2014, ApJ, 784, 58
Smit, R., Bouwens, R. J., Franx, M., et al. 2015, ApJ, 801, 122
Smith, A., Kannan, R., Garaldi, E., et al. 2022, MNRAS, 512, 3243
Smith, A., Ma, X., Bromm, V., et al. 2019, MNRAS, 484, 39
Sobral, D., Matthee, J., Best, P., et al. 2017, MNRAS, 466, 1242
Stark, D. P. 2016, ARA&A, 54, 761
Stark, D. P., Ellis, R. S., Chiu, K., Ouchi, M., & Bunker, A. 2010, MNRAS, 408, 1628
Stark, D. P., Walth, G., Charlot, S., et al. 2015, MNRAS, 454, 1393
Stark, D. P., Ellis, R. S., Charlot, S., et al. 2017, MNRAS, 464, 469
Stefanon, M., Bouwens, R. J., Illingworth, G. D., et al. 2022, ApJ, 935, 94
Steidel, C. C., Erb, D. K., Shapley, A. E., et al. 2010, ApJ, 717, 289
Tang, M., Stark, D. P., Chevallard, J., & Charlot, S. 2019, MNRAS, 489, 2572
Tang, M., Stark, D. P., Chevallard, J., et al. 2021a, MNRAS, 503, 4105
Tang, M., Stark, D. P., Chevallard, J., et al. 2021b, MNRAS, 501, 3238
Tang, M., Stark, D. P., & Ellis, R. S. 2022, MNRAS, 513, 5211
Tang, M., Stark, D. P., Chen, Z., et al. 2023, MNRAS, 526, 1657
Tang, M., Stark, D. P., Ellis, R. S., et al. 2024, MNRAS, 531, 2701
Tilvi, V., Malhotra, S., Rhoads, J. E., et al. 2020, ApJL, 891, L10
Topping, M. W., Stark, D. P., Endsley, R., et al. 2022, MNRAS, 516, 975
Topping, M. W., Stark, D. P., Senchyna, P., et al. 2024, MNRAS, 529, 3301
Trainor, R. F., Steidel, C. C., Strom, A. L., & Rudie, G. C. 2015, ApJ, 809, 89
Trebitsch, M., Blaizot, J., Rosdahl, J., Devriendt, J., & Slyz, A. 2017, MNRAS, 470, 224
Treu, T., Roberts-Borsani, G., Bradac, M., et al. 2022, ApJ, 935, 110
Umeda, H., Ouchi, M., Nakajima, K., et al. 2023, arXiv:2306.00487
Vanzella, E., Nonino, M., Cupani, G., et al. 2018, MNRAS, 476, L15
Verhamme, A., Orlitová, I., Schaerer, D., & Hayes, M. 2015, A&A, 578, A7
Verhamme, A., Orlitová, I., Schaerer, D., et al. 2017, A&A, 597, A13
Verhamme, A., Schaerer, D., Atek, H., & Tapken, C. 2008, A&A, 491, 89
Verhamme, A., Schaerer, D., & Maselli, A. 2006, A&A, 460, 397
Virtanen, P., Gommers, R., Oliphant, T. E., et al. 2020, NatMe, 17, 261
Wang, F., Davies, F. B., Yang, J., et al. 2020, ApJ, 896, 23
Weinberger, L. H., Kulkarni, G., Haehnelt, M. G., Choudhury, T. R., & Puchwein, E. 2018, MNRAS, 479, 2564
Whitler, L., Endsley, R., Stark, D. P., et al. 2023a, MNRAS, 519, 157
Whitler, L., Stark, D. P., Endsley, R., et al. 2023b, MNRAS, 519, 5859
Witstok, J., Maiolino, R., Smit, R., et al. 2024, arXiv:2404.05724
Wyithe, J. S. B., & Loeb, A. 2005, ApJ, 625, 1
Yang, H., Malhotra, S., Rhoads, J. E., & Wang, J. 2017, ApJ, 847, 38
Yang, J., Wang, F., Fan, X., et al. 2020a, ApJL, 897, L14
Yang, J., Wang, F., Fan, X., et al. 2020b, ApJ, 904, 26
Zheng, Z.-Y., Wang, J., Rhoads, J., et al. 2017, ApJL, 842, L22
Zhu, Y., Becker, G. D., Christenson, H. M., et al. 2023, ApJ, 955, 115
Zitrin, A., Labbé, I., Belli, S., et al. 2015, ApJL, 810, L12